Author/s:
Swiderski, K;Chan, AS;Herold, MJ;Kueh, AJ;Chung, JD;Hardee, JP;Trieu, J;Chee, A;Naim, T;Gregorevic, P;Lynch, GS

Title:
The BALB/c.mdx62 mouse exhibits a dystrophic muscle pathology and is a model of Duchenne muscular dystrophy

Date:
2024

Citation:
Swiderski, K., Chan, A. S., Herold, M. J., Kueh, A. J., Chung, J. D., Hardee, J. P., Trieu, J., Chee, A., Naim, T., Gregorevic, P. & Lynch, G. S. (2024). The BALB/c.mdx62 mouse exhibits a dystrophic muscle pathology and is a model of Duchenne muscular dystrophy. DMM Disease Models and Mechanisms, 17 (4), https://doi.org/10.1242/dmm.050502.

Persistent Link:
https://hdl.handle.net/11343/345392

The BALB/c.*mdx*62 mouse exhibits a dystrophic muscle pathology and is a novel model of Duchenne muscular dystrophy

Kristy Swiderski[1], Audrey S. Chan[1], Marco J. Herold[2,3,4,5], Andrew J. Kueh[2,3,4,5], Jin D. Chung[1], Justin P. Hardee[1], Jennifer Trieu[1], Annabel Chee[1], Timur Naim[1], Paul Gregorevic[1], and Gordon S. Lynch[1,*]

[1]Centre for Muscle Research, Department of Anatomy and Physiology, The University of Melbourne, VIC, Australia, 3010
[2]The Walter and Eliza Hall Institute of Medical Research, Parkville, VIC, Australia
[3]Department of Medical Biology, The University of Melbourne, Melbourne, Victoria, Australia
[4]Olivia Newton-John Cancer Research Institute, Heidelberg, Victoria, Australia
5School of Cancer Medicine, La Trobe University, Heidelberg, Victoria 3084, Australia

[*]Correspondence: gsl@unimelb.edu.au

Keywords: muscular dystrophy, skeletal muscle, bone, pathophysiology, preclinical, genetic modifier

Summary statement

Characterization of a novel DMD mouse model, the first in BALB/c mice, with a CRISPR-induced deletion within exon 62 of the *Dmd* gene exhibiting dystrophic skeletal muscle pathology and an associated bone phenotype.

Abstract

Duchenne muscular dystrophy (DMD) is a devastating monogenic skeletal muscle wasting disorder. While many pharmacological and genetic interventions have been reported in preclinical studies, few have progressed to clinical trials with meaningful benefit. Identifying therapeutic potential may be limited by availability of suitable preclinical mouse models. More rigorous testing across models with varied background strains and mutations may identify treatments for clinical success. Here we report the generation of a DMD mouse model, with a CRISPR-induced deletion within exon 62 of the *Dmd* gene, and the first generated in BALB/c mice. Analysis of mice at 3, 6, and 12 months of age confirmed loss of

Dp427 protein expression and resultant dystrophic pathology in limb muscles and the diaphragm, with evidence of centrally nucleated fibers, increased inflammatory markers and fibrosis, progressive decline in muscle function, and compromised trabecular bone development. The C.*mdx*62 mouse is a novel model of DMD with associated variations in the immune response and muscle phenotype, compared with existing models. It represents an important addition to the preclinical model toolbox for developing therapeutic strategies.

Introduction

Duchenne muscular dystrophy (DMD) is an X-linked genetic muscle wasting disorder arising from mutations in the dystrophin (*Dmd*) gene resulting in aberrant expression of the dystrophin protein and affecting 1:3500-6000 live male births worldwide, with an overall prevalence of less than 10 cases per 100,000 males (Bushby et al., 2010, Duan et al., 2021, Hoffman et al., 1987). In skeletal muscle, the dystrophin (Dp427) protein forms part of a sarcolemmal multimeric protein complex termed the dystrophin glycoprotein complex (DGC) which links the extracellular matrix to the internal muscle fiber actin cytoskeleton to mediate the forces of contraction (Ervasti and Campbell, 1993), and acts a hub for signaling activity that may regulate muscle proteostasis (Acharyya et al., 2005, Garbincius and Michele, 2015, Langenbach and Rando, 2002, Xiong et al., 2009). In the absence of dystrophin, the DGC fails to accumulate at the sarcolemma, resulting in membrane fragility, microtearing upon contraction, and initiating events that ultimately lead to fiber degeneration and muscle wasting.

Despite the cause of DMD being attributed to mutations in dystrophin after identification of the *Dmd* gene in 1987, treatment options have been limited to corticosteroid therapy via administration of prednisone/prednisolone, deflazacort (approved by the FDA in 2017), and more recently vamorolone (AGAMREE; approved by the FDA and EMA in 2023). However, while corticosteroid therapies delay disease progression and improve ambulation and lifespan in DMD patients, their chronic use is associated with significant side effects including impacts on height, body mass, and bone health, although these effects may be somewhat reduced with vamorolone (Grounds and Lloyd, 2023). The past decade has seen the advent of the first dystrophin restoration therapies, with FDA approval of exon skipping drugs Exondys 51 (eteplirsen) in 2016, VYONDYS 53 (golodirsen) in 2019, Viltepso (viltolarsen) in 2020, and Amondys 45 (casimersen) in 2021, for exon 51, 53, and 45 skipping, respectively. While

a significant and exciting advance for DMD, these therapies remain expensive and restricted to patients with specific mutations. The FDA also recently approved adeno-associated virus (AAV) gene therapy for DMD in 2023 (Elevidys), but the long-term clinical benefits of these gene replacement therapies have yet to be evaluated. There remains no cure or effective treatment for a large majority of patients (Hoffman, 2020).

As a monogenic disorder, the ultimate cure for DMD will come from correcting the underlying genetic defect, and preclinical studies in animal models of DMD are essential for testing various viral and non-viral genetic strategies to restore dystrophin expression. Such studies using compounds to induce read-through of premature stop codons or skipping of mutated exons (Barton-Davis et al., 1999, Lu et al., 2003), and viral vectors to re-express dystrophin mini-genes, have rescued the dystrophic phenotype in murine and canine models (Blankinship et al., 2006, Bostick et al., 2012, Duan, 2018, Fabb et al., 2002, Gregorevic et al., 2004, Liu et al., 2005, Wang et al., 2007), with some proceeding to clinical trials and the approval of genetic modifiers to treat DMD (Bitetti et al., 2021, Dunant et al., 2003, Malik et al., 2010, Mercuri et al., 2020, Michorowska, 2021, Pasca et al., 2022, Ruggiero et al., 2018). Therefore, rigorous preclinical models that recapitulate the dystrophic pathology in patients remain critical to developing treatments for DMD.

The C57BL/10ScSn *mdx* mouse, harboring a naturally-occurring point mutation in exon 23 of the *Dmd* gene, is the most commonly studied preclinical model of DMD. While genetically similar to DMD, the mice have a mild phenotype due to compensatory upregulation of a homologous protein, utrophin (Deconinck et al., 1998, Rafael et al., 1998, Tinsley et al., 1998). To generate a murine model lacking both dystrophin and utrophin, the utrophin gene was deleted from the C57BL/10ScSn *mdx* mouse, and while these *mdx*/*utrn*$^{-/-}$ or *dko* mice are no longer genetically similar to DMD, their phenotype more closely resembles the disease progression in patients (Deconinck et al., 1998). The C57BL/10ScSn *mdx* mouse has also been bred onto the DBA2/J mouse strain, referred to as the D2.*mdx* mouse. These mice also exhibit a more severe muscle pathology than C57BL/10ScSn *mdx* mice which has been attributed to a mutation in the *Ltbp4* gene in the DBA2/J mouse that enhances TGF-β signaling and fibrosis (Coley et al., 2016).

As all these models originate from the C57LB/10ScSn *mdx* mouse, they contain the same dystrophin mutation in exon 23, which results in an absence of the full length Dp427 dystrophin protein isoform but does not affect expression of other isoforms. To assess the impact of mutations across the gene, affecting different dystrophin isoforms, chemical

mutagenesis has been utilized to generate the *mdx*^{2cv}, *mdx*^{3cv}, *mdx*^{4cv}, and *mdx*^{5cv} mouse models (Cox et al., 1993). In addition, gene targeting to delete exon 52 in C57BL/6J mice (*mdx*52), resulted in the absence of Dp427, Dp260, and Dp140 with the expected dystrophic pathology (Araki et al., 1997).

Each of these models has advantages and disadvantages for use in preclinical studies, and there is no one perfect preclinical murine model for studying DMD. However, given the sheer number of DMD-causative mutations and since the human population is heterogenous, something not generally modeled in mouse studies, the use of multiple models in combination provides a powerful approach to assess treatment efficacy in mice with different mutation locations, disease severity, and genetic background. To this end, we created a novel dystrophin-deficient mouse generated by CRISPR-Cas9 in BALB/c mice termed C.*mdx*$^{emDel9418\text{-}9425}$ (hereafter referred to as C.*mdx*62) with an 8 bp deletion in the coding sequence of the *Dmd* gene, mapping to exon 62. In this study, we have characterized its skeletal muscle and bone phenotypes that identify it as a useful murine model of DMD.

Results

Dystrophin mutant mice lack Dp427 protein expression

CRISPR/Cas9 technology was utilized with sgRNA designed to introduce point mutations in exon 62 of the dystrophin (*Dmd*) gene, which forms part of the WW domain of the dystrophin protein, a region of interest that directly regulates the interaction between dystrophin and β-dystroglycan (Swiderski et al., 2021, Swiderski et al., 2014). In screening for these mutations, a small insertion/deletion (indel) was identified in which 8 bp were deleted in exon 62, just upstream of the mutations reported in the *mdx*^{3cv} and *mdx*$^{\beta geo}$ mouse models (Fig. 1A). Analysis of patient mutations at this site demonstrated an association with a DMD phenotype (Unique variants in the DMD gene – Global Variome shared LOVD), and analysis with a reading frame checker indicated a frameshift mutation likely to result in degradation of the protein product. Histological analysis via hematoxylin and eosin staining confirmed the expected dystrophic pathology in the TA muscles and diaphragm of 3-month-old mice (Fig. 1B), with the presence of inflammatory infiltrate, variable fiber sizes, and centrally nucleated fibers. Western immunoblotting confirmed the absence of the dystrophin Dp427 protein isoform from the gastrocnemius muscle, with a subsequent reduction in the overall expression of the β-dystroglycan protein (Fig. 1C, D). No change in the level of

utrophin protein expression was detected (Fig. 1C, D). Western immunoblotting extracts from the sciatic nerve confirmed the loss of Dp116 expression but maintenance of Dp71 and Dp40 expression as expected, based on the location of the mutation (Supp. Fig. S1). Immunofluorescence analyses confirmed the absence of dystrophin protein at the sarcolemma of fibers in the TA muscle (Fig. 1E) and diaphragm (Fig. 1F), with decreased sarcolemmal localization of the associated DGC proteins, β-dystroglycan, α-sarcoglycan, and α1-syntrophin (Fig. 1E, F). Consistent with western immunoblotting, no increase in utrophin protein expression was observed in the TA muscles (Fig. 1E) or diaphragm (Fig. 1F) of C.*mdx*62 mice, with expression co-localizing to the neuromuscular junction, as indicated by staining for the acetylcholine receptor (AChR).

Dystrophin mutant mice exhibit skeletal muscle hypertrophy

BALB/c WT and C.*mdx*62 mutant mice were killed at 3, 6, and 12 months of age to characterize the skeletal muscle phenotype. Relative to WT BALB/c mice, C.*mdx*62 mice tended to be heavier, with significantly greater body mass at 3 and 6 months of age, and no change in body mass at 12 months of age (Fig. 2A). Normalized masses of TA and soleus muscles from C.*mdx*62 mice were heavier than those from WT mice at all ages studied (Fig. 2B, C). EDL muscles from C.*mdx*62 mice were smaller at 3 months of age, not different at 6 months of age, but heavier at 12 months of age relative to WT mice (Fig. 2D). Gastrocnemius muscles from C.*mdx*62 mice were not different in mass from those muscles of WT mice at any age (Fig. 2E). Normalized heart mass was not different between WT and C.*mdx*62 mice at 3 months of age but was lower at 6 and 12 months of age in C.*mdx*62 mice relative to WT mice (Fig. 2F), even when the two abnormally large WT hearts were removed (Supp. Fig. S2). Consistent with previous reports in *mdx* mice, C.*mdx*62 mice had reduced epididymal fat mass at all ages studied (Fig. 2G). C.*mdx*62 mice had larger spleens (Fig. 2H) and livers (Fig. 2I) at 3 months of age with no difference at 6 or 12 months of age. Serum analysis confirmed increased AST levels (Fig. 2J) in 3-, 6-, and 12-month-old C.*mdx*62 mice relative to WT mice. Together, these data confirmed the C.*mdx*62 mice had typical features of dystrophic pathology.

*Muscles of C.*mdx*62 mice have an increased susceptibility to contraction-mediated damage*

Force production and the loss of force after repeated lengthening contractions were assessed in TA muscles from 3-, 6-, and 12-month-old C.*mdx*62 mice relative to age-matched BALB/c WT mice. Twitch (Fig. 3A) and tetanic forces (Fig. 3B) were higher in C.*mdx*62 mice at 6 months but not at 3 or 12 months of age relative to WT mice. When normalized for changes in muscle cross-sectional area, specific force was lower in C.*mdx*62 mice relative to WT mice at 3 and 12 months but not at 6 months of age (Fig. 3C). Time-to-peak tension (TPT; Fig. 3D) was faster only at 6 months of age, and one-half relaxation time (½RT; Fig. 3E) was faster at 3 and 6 months but not different at 12 months of age in C.*mdx*62 mice relative to WT, with the rate of twitch contraction (dP/dt) increased relative to WT only at 6 months of age (Fig. 3F). Analysis of fiber type proportions showed a shift towards a faster phenotype with a reduction in the proportion of type IIa fibers in TA muscles of C.*mdx*62 mice at 6 and 12 months of age (Supp. Fig. S3A-D), increased size of IIa and IIb fibers at 6 months at 12 months of age, respectively (Supp. Fig. S3A, E-G), but no change in fiber oxidative capacity based on SDH reaction intensity (Supp. Fig. S3H-K).

Frequency-force analyses revealed muscles from 3- and 6-month-old C.*mdx*62 mice produced less force at lower frequencies (Fig. 3G, H), but 6-month-old C.*mdx*62 mice produced greater force at higher frequencies (above 100 Hz) relative to muscles from WT mice (Fig. 3H). Force production was similar at all stimulation frequencies between 12-month-old WT and C.*mdx*62 mice (Fig. 3I). Normalized force production was reduced in muscles from C.*mdx*62 mice relative to WT mice at 3-, 6-, and 12-months-old (Fig. 3J-L; $P < 0.01$, $P < 0.001$, $P < 0.0001$ genotype main effect respectively) with post-hoc analyses confirming reduced force production at lower frequencies at all ages (Fig. 3J-H) but only at higher frequencies at 3- (Fig. 3J) and 12-months (Fig. 3L).

A key feature of dystrophin deficiency is a higher susceptibility to contraction-induced injury based on significantly higher force deficits after repeated lengthening contractions. When TA muscles were stretched by up to 30% of fiber length, the force deficit for 3-, 6-, and 12-month-old WT mice averaged 4%, 3%, and 19%, respectively, compared with TA muscles from 3-, 6-, and 12-month-old C.*mdx*62 mice, with average force deficits of 24%, 44%, and 61% from the initial (uninjured) force, respectively (Fig. 3M-O). It is worth noting that the function data for the 12-month-old WT mice was restricted to only 3 mice due to the unexpected death of 2 mice with calcified hearts. These data should therefore be considered as preliminary. Further comparisons between 12-month-old WT and C.*mdx*62 mice are

warranted with additional WT mice. Overall, muscles from C.*mdx*62 mice were more susceptible to contraction-induced injury, and the force deficits were exacerbated with age.

Skeletal muscles from C.mdx62 mice exhibit a dystrophic pathology

The loss of dystrophin from skeletal muscle is well-characterized to reduce membrane stability and result in ongoing cycles of degeneration and regeneration, evident from the increased prevalence of centrally-nucleated fibers. To assess these parameters in C.*mdx*62 mice, IgG infiltration, central nucleation, and fibrosis were assessed in the TA muscle and diaphragm. The number of IgG positive fibers was increased in TA muscles of C.*mdx*62 mice ($P < 0.01$ genotype main effect) with a trend towards a higher proportion at 3 months ($P = 0.16$; Fig. 4A, D), 6 months ($P = 0.07$; Fig. 4B, D) and 12 months ($P = 0.22$; Fig. 4C, D) relative to WT mice. Immunostaining with laminin and the nuclear stain DAPI detected very few centrally-located fibers in TA muscles from WT mice at 3 months (Fig. 4A, E), 6 months (Fig. 4B, E), and 12 months of age (Fig. 4C, E). Conversely, the proportion of fibers with centrally-located nuclei increased to 40% in TA muscles of 3 month old C.*mdx*62 mice (Fig. 4A, E), 48% at 6 months (Fig. 4B, E), and 59% at 12 months (Fig. 4C, E), within the expected range reported in *mdx* mice (Coley et al., 2016), and as outlined in the standard operating protocols published by TREAT-NMD (SOP DMD_M.1.2.001). Similarly, fibrosis was higher at 3 months (Fig. 4A, F) and 6 months (Fig. 4B, F) in TA muscles of C.*mdx*62 mice relative to WT, with a similar trend towards an increase at 12 months ($P = 0.0877$; Fig. 4C, F). Analysis of laminin-stained sections also confirmed an increase in myofiber size at 6 and 12 months of age in TA muscles of C.*mdx*62 mice (Supp. Fig. S4A), which was attributed to the increased proportion of both smaller and larger muscle fibers at all ages (Supp. Fig. S4B-D).

In the diaphragm, the proportion of IgG positive fibers (Fig. 5A-C, D), central nuclei (Fig. 5A-C, E), and fibrosis (Fig. 5A-C, F), were significantly higher in C.*mdx*62 mice relative to WT at all ages. Together, these data confirm significant dystrophic pathology up to 12 months of age in the limb and diaphragm muscles of C.*mdx*62 mice.

As dystrophic pathology also affects the heart, gene and protein expression markers of cardiac damage were assessed in WT and C.*mdx*62 mice at 3, 6, and 12 months of age. Western immunoblotting analysis of phospholamban phosphorylation showed a trend for increased phosphorylation in hearts from 3-month-old C.*mdx*62 mice ($P = 0.07$; Supp. Fig.

S5A), and reduced phosphorylation in hearts from 6-month-old C.*mdx*62 mice relative to WT (Supp. Fig. S5A). Phospholamban phosphorylation was reduced in WT and C.*mdx*62 hearts at 12 months of age (Supp. Fig. S5A). Together, these data support earlier reductions in SERCA function in the hearts of C.*mdx*62 mice relative to WT (Voit et al., 2017). Consistent with previous reports in BALB/c mice, two of the 12-month-old mice had calcified atria, which was not observed in any of the C.*mdx*62 mice (data not shown). Gene expression analyses of markers of osteogenesis showed a main effect for increased *Runx2* expression with both increasing age and in C.*mdx*62 mice ($P < 0.05$ age main effect; $P < 0.01$ genotype main effect; Supp. Fig. S4B), but no change in either *Ocn* (Supp. Fig. S5C) or *Alp* (Supp. Fig. S5D) expression. Markers of inflammation and fibrosis showed no changes in expression of *F4/80* (Supp. Fig. S5E), *TGFβ* (Supp. Fig. S5F), *Col1a1* (Supp. Fig. S5G), *Col3a1* (Supp. Fig. S5H), or *Col6a1* (Supp. Fig. S5I). These preliminary findings suggest the C.*mdx*62 mouse may have a cardiac phenotype from 6 months of age, but more extensive histological and functional analyses are required to assess this pathology.

Myofiber ossification in diaphragm of C.mdx62 mice

Calcifications within muscle have been reported in the more severely affected diaphragm, and in mouse models of DMD missing multiple dystrophin isoforms (Young et al., 2020). To determine whether calcification was evident, TA (Fig. 6A) and diaphragm muscles (Fig. 6B) from 3, 6, and 12 month old WT and C.*mdx*62 mice were stained with Alizarin red. Calcification was not observed in TA or diaphragm muscles from WT mice, but some areas of calcification were evident in TA muscles from C.*mdx*62 mice at all ages ($P < 0.01$ genotype main effect; Fig. 6A, C). Significant calcification was present in the diaphragm of C.*mdx*62 mice at 3, 6, and 12 months of age, which was reduced with increasing age ($P < 0.05$ age main effect; Fig. 6B, D).

*C.*mdx*62 mice exhibit deficits in trabecular bone development*

To characterize the bone phenotype in this model, we used micro-computed tomography to assess trabecular bone within the proximal tibia (Fig. 7A). There was no difference in trabecular bone volume ratio (Fig. 7B) or trabecular number (Fig. 7C) between WT and C.*mdx*62 mice at 3 months of age. However, while trabecular bone development continued in WT mice between 3 and 6 months of age, trabecular bone mass and number were unchanged

in C.*mdx*62 (Fig. 7B, C). At 12 months of age, as expected, WT mice exhibited age-related trabecular bone loss, evident from a decrease in trabecular bone volume ratio and number and increased trabecular separation (Fig. 7B-D). The loss of trabecular bone between 6 and 12 months of age was attenuated in C.*mdx*62 mice, and they exhibited more trabecular bone mass than age-matched WT mice.

We then assessed cortical bone at the tibial mid-diaphysis (Fig. 7F). As for the trabecular bone, there was no difference in cortical bone parameters at 3 months of age. However, at 6 months of age, C.*mdx*62 mice had a significantly larger diaphysis (Fig. 7G) and at 12 months of age, had a greater normalized bone area (Fig. 7H), areal tissue mineral density (Fig. 7I), and cortical thickness (Fig. 7J) than the age-matched counterparts. There was no difference in shape ratio (Chadwick et al., 2018) (Fig. 7K) or resistance to torsional forces (Fig. 7L), at any age. Finally, and in light of our recent studies examining the influence of muscle mass on tibial geometry (Chan et al., 2023, Chan et al., 2021), we also found augmentation of the tibial crest in C.*mdx*62 mice due to the larger, adjacent TA muscle (Supp. Fig. S6). Collectively, these data indicate that skeletal development and structure are also affected in this murine model of DMD, with prominent effects on trabecular bone microstructure.

Discussion

Small animal models are essential tools for the development and preclinical testing of potential therapies for DMD. The gold standard and most widely used murine model is the *mdx* mouse, which genocopies the human disease but has only a mild skeletal muscle pathology with the exception of the diaphragm (Swiderski and Lynch, 2021). A number of other murine models have been generated that either lack additional related proteins (e.g. utrophin), have mutations at different sites in the dystrophin gene (e.g. $mdx^{2\text{-}5cv}$, *mdx52*, $mdx^{\beta geo}$), or result from crossing the *mdx* mouse onto different genetic backgrounds (e.g. D2.*mdx*) (Swiderski and Lynch, 2021). Importantly, no one model perfectly replicates the DMD pathology, but utilizing a combination of models with different disease severities is a powerful approach for interrogating novel treatments. The generation of novel mouse models with varying mutation sites and a different genetic background, enhances these interrogative tools for DMD. To this end, we identified an indel during a CRISPR-based mutation screen resulting in an 8 bp deletion within exon 62 of the *Dmd* gene in BALB/c mice. Analysis of

these mice at 3, 6, and 12 months of age confirmed the expected dystrophic pathology in the limb muscles and diaphragm, as well as compromised trabecular bone development. This new murine model is therefore a useful addition to the preclinical model toolbox for the development and testing of novel therapies for DMD.

A dystrophic muscle phenotype like that in *mdx* mice was confirmed, with evidence for limb muscle hypertrophy, centrally nucleated variably-sized muscle fibers, and increased fibrosis and membrane permeability. Limb muscle hypertrophy has been extensively reported in the C57BL/10ScSn *mdx* mouse and is generally attributed to a robust regenerative response (Coley et al., 2016, Duddy et al., 2015). This phenotype is not typically observed in the *mdx*/*utrn*$^{-/-}$ (Deconinck et al., 1997, Ham et al., 2019) or D2.*mdx* mouse (Coley et al., 2016), which usually exhibit more of an atrophic phenotype. Interestingly, the C.*mdx*62 presents with a phenotype intermediate to these models with hypertrophy of the TA and soleus muscles, variable changes in mass of the EDL, and no change in the gastrocnemius. The mechanism responsible for these muscle specific changes remains to be determined and should be explored in future studies using genomic and proteomic profiling to detect specific differences between muscle groups.

Absolute force production was maintained in the TA muscles of C.*mdx*62 mice relative to WT mice at 3 and 12 months of age and increased at 6 months of age. Like C57BL/10ScSn *mdx* mice, this likely resulted from increased muscle mass as normalized force was lower relative to WT mice (Lynch et al., 2001, Sacco et al., 1992). Interestingly, normalized force was not different between WT and C.*mdx*62 mice at 6 months of age, but this was likely due to reduced force in the WT mice since normalized force was stable across the 3-, 6-, and 12-month age groups in the C.*mdx*62 mice but changed with age in the WT mice. As the WT mice used in this study were purchased separately, and therefore did not exactly match the genetics of the C.*mdx*62 mice, future studies should incorporate littermate controls to eliminate this confounding factor.

As reported previously in preclinical models and in DMD patients (Swiderski and Lynch, 2021), the pathology was more significant in the diaphragm than in limb muscles. This was confirmed by significant ectopic myofiber calcification in the diaphragm of C.*mdx*62 mice at all ages relative to WT mice, like that reported previously in *mdx*$^{\beta geo}$ and D2.*mdx* mice (Hammers et al., 2020, Mazala et al., 2020, van Putten et al., 2019, Young et al., 2020). In the diaphragm muscles of D2.*mdx* mice, ectopic myofiber calcification has been attributed to a polymorphism in the *Ltbp4* gene from crossing the *mdx* mouse onto the DBA/2J strain (Coley

et al., 2016). BALB/c mice exhibit dystrophic cardiac calcinosis of the epicardia and are more susceptible to developing ectopic calcification (Eaton et al., 1978). The increased ectopic myofiber calcification in the diaphragm of C.*mdx*62 mice may therefore be attributed to the BALB/c strain background. Alternatively, the worsened phenotype may arise from the loss of additional dystrophin isoforms, as was suggested in the *mdx*$^{\beta geo}$ mouse which lacks all dystrophin isoforms (Young et al., 2020), but this remains to be confirmed.

The characterization of the C.*mdx*62 mouse presented here demonstrates the expected dystrophic pathology in the limb muscles and diaphragm. However, respiratory and cardiac failure are the two most common causes of death in DMD (Mercuri et al., 2019), and these are less well modelled in mice. Like DBA mice, BALB/c mice are prone to dystrophic cardiac calcinosis (Glass et al., 2013). In fact, two of the five 12-month-old WT BALB/c mice in the present study exhibited significant cardiac calcification. Interestingly, hearts from 12-month-old C.*mdx*62 mice studied here exhibited signs of fibrosis at dissection, but with the exception of a main effect for increased *Runx2* expression, there was no evidence of ectopic cardiac calcification in these mice. The presence of a cardiac phenotype in WT BALB/c mice may influence the interpretation of any phenotype in the C.*mdx*62 mouse. Our preliminary characterization suggests the C.*mdx*62 mouse may have a cardiac phenotype from 6 months of age, indicated by a reduced heart mass and SERCA dysfunction. Reduced heart mass has similarly been observed in *mdx*/*utrn*$^{-/-}$ mice (Kennedy et al., 2016), and increased heart mass has been reported to occur at least transiently in D2.*mdx* mice with no change in C57BL/10ScSn *mdx* mice up to approximately 6 months of age (Kennedy et al., 2018). Future studies examining cardiac histology, cardiac function, and respiratory capacity are required to determine whether the C.*mdx*62 model develops a cardiorespiratory phenotype and how this relates to the spectrum of phenotypes in existing models.

Poor bone health is a common yet serious complication of pediatric neuromuscular diseases, including, but not limited to, spinal muscular atrophy (SMA) (Vai et al., 2015), cerebral palsy (Modlesky et al., 2009), myelomeningocele (Chadwick et al., 2018), and DMD. Reduced mobility and other systemic factors, lead to a common presentation of abnormal bone development and architecture, with low bone mass and mineral density (Veilleux and Rauch, 2017). In DMD, up to 20-25% of patients experience a long bone fracture (McDonald et al., 2002), with those occurring in the lower extremities often leading to a permanent loss of ambulation (Larson and Henderson, 2000). Furthermore, the osteotoxic effects of chronic glucocorticoid therapy significantly increases the prevalence of vertebral fractures (King et

al., 2007, Ward et al., 2018). While the pathophysiological mechanisms driving poor bone health are unclear, it remains important to understand and identify effective avenues to improve the quality of life for patients. We report here that the C.*mdx*62 mouse model exhibits compromised trabecular bone development and accrual during the later stages of skeletal development and maturation (i.e., after 3-months of age). This is a likely consequence of the increased inflammation and dystrophic phenotype of the skeletal muscle and is consistent with previous reports in *mdx* mice (Nakagaki et al., 2011, Novotny et al., 2011, Ponzetti et al., 2022, Rufo et al., 2011, Wada et al., 2019). Interestingly, the age-related loss of trabecular bone was attenuated in older C.*mdx*62 mice and while interesting, the underlying mechanism for this remains unclear and warrants further investigation.

Unlike our observations of the trabecular bone, the C.*mdx*62 mouse model did not exhibit a cortical bone phenotype that is reminiscent of that observed in DMD patients. The C.*mdx*62 mouse exhibits age-related increases in cortical bone mass, diameter, thickness, and tissue mineral density, relative to their wildtype counterpart. The effect of muscular dystrophy on cortical bone has been less clear, with some studies reporting *mdx* mice having more slender, thinner, and weaker cortical bone (Anderson et al., 1993, Nakagaki et al., 2011, Novotny et al., 2011, Rufo et al., 2011, Wada et al., 2019), while others have reported no differences in cortical thickness or diameter (Wood et al., 2020), as well as increased bone mineral density (Montgomery et al., 2005). These inconsistencies could be due to the different ages, sex, and region of long bone analysed, and it remains difficult to define the pathophysiological mechanism(s) underlying the influence of dystrophic muscle on the skeleton. While our data suggests these structural (extrinsic) changes to cortical bone would improve bone strength, this remains to be confirmed through mechanical testing. Nevertheless, we propose the potential use of the C.*mdx*62 mouse as a tool to identify modifiable and/or protective factors that may be absent in *mdx* mice on the C57BL/10 background strain.

We also report that bone retains the ability to structurally adapt to the adjacent skeletal musculature, independent of the dystrophic phenotype of C.*mdx*62 mice. We propose that the lengthening of the tibial crest in C.*mdx*62 mice is the direct result of the larger TA muscle. We previously reported this phenomenon in healthy mice in response to follistatin-induced muscle hypertrophy (Chan et al., 2021) and in dystrophic mice after muscle remodeling (Chan et al., 2023). These findings are akin to a previous study reporting expansion of the third trochanter in response in *mdx* mice (Montgomery et al., 2005), and in myostatin-null mice (Hamrick et al., 2000, Hamrick et al., 2002). We propose that the deficit in trabecular

bone development is predominantly driven by the dystrophic muscle phenotype, while the differences in cortical bone structure are likely an adaptive response to accommodate the larger, adjacent musculature. We speculate there are two possibilities that could account for the differential phenotypes between trabecular and cortical bone. Firstly, the rate of bone modeling and remodeling differ between these two compartments, with trabecular bone being more susceptible to imbalances in formation and resorption due to its higher turnover rate and larger surface area-to-volume ratio. Secondly, dystrophin may play an intrinsic role in bone-resident cell types. While this has not been confirmed, it remains interesting and worthy of further investigation. Collectively, our data add merit to the C.*mdx*62 mouse being a unique and valuable model for investigating common and divergent mechanisms across mouse strains, as well as being a suitable model for studying the rapid loss of trabecular bone as a consequence of glucocorticoid therapy (Tung et al., 2021).

CRISPR/Cas9 has been increasingly utilized to generate murine DMD models with mutations in specific regions. The advent of CRISPR/Cas9 technology provided a more simple and less time-consuming approach for generating novel models with mutations in specific regions for targeted study, with some mimicking patient mutations or humanizing the mouse gene, for preclinical evaluation of targeted exon skipping and/or gene editing therapies (Amoasii et al., 2017, Kim et al., 2017, Koo et al., 2018, Maino et al., 2021, Min et al., 2019, Min et al., 2020, Rok et al., 2023, Ryu et al., 2018, Wong et al., 2020, Zhang et al., 2020). The majority of these models have been generated in C57BL/6J mice (or in strains crossed to C57BL/6J to generate a mixed background), with only a few examples in other backgrounds, including an exon 51 deletion in C57BL/6N mice (Chemello et al., 2020), and mouse models expressing mutations in the humanized *dmd* gene in C57BL/10, DBA2, or C57BL/6J mice (Kenjo et al., 2021, Pickar-Oliver et al., 2021, Young et al., 2017). Like the C.*mdx*62 mouse, all these models exhibit an expected dystrophic pathology for mutations resulting in the loss of full-length dystrophin protein expression. The C.*mdx*62 represents a novel mouse model with both a different mutation location and background strain.

The 8 bp deletion in exon 62 in these mice should affect expression of all dystrophin isoforms, with the exception of Dp71 and Dp40, for which the promoter is located in intron 62 (Hugnot et al., 1992, Lederfein et al., 1993, Rapaport et al., 1992), just downstream of this mutation. Analysis of sciatic nerve protein extracts confirmed the loss of Dp116 expression in these mice. Loss of Dp260 and Dp140 could not be confirmed due to the inability to detect these isoforms in the brains of the BALB/c WT mice but can be implied based on the

locations of the promoters for these isoforms. There is potential for non-muscle phenotypes in these mice, such as those reported previously in *mdx*52 mice (Barboni et al., 2021, Saoudi et al., 2021). Importantly, this is the first mouse model with a mutation at exon 62. Given that mutations in this region result in the DMD phenotype, with mutations in exon 62 accounting for 0.64% of reported variants in UMD-TREAT-NMD database (Unique variants in the DMD gene – Global Variome shared LOVD; http://umd.be/TREAT_DMD/), this mouse may prove to be an important tool for testing exon skipping strategies relevant to exon 62 gene mutations.

While multiple murine models of DMD have been generated using various strategies in the C57BL/6, C57BL/10, and DBA/2J mouse strains, this is the first model, to our knowledge, characterized in the BALB/c mouse strain. Since the immunological phenotype of BALB/c mice varies relative to C57BL/6 mice, with stronger Th2 and humoral responses (Watanabe et al., 2004), it is likely that mice on a BALB/c background respond differently to therapeutic interventions. Individual immune responses vary greatly in the human population and immune response variability to some therapies, particularly viral-mediated interventions, has led to a shortfall in successful translation to the clinic and may limit the dose that can be safely administered to patients. Furthermore, the skeletal muscles of BALB/c mice have been reported to have a reduced regenerative capacity after femoral artery ligation compared to C57BL/6 mice (Tu et al., 2022), and so it may be expected that the dystrophic progression could vary between different mouse strains. Preclinical analysis of interventions in DMD mouse models across multiple background strains with varying immune profiles and regenerative capacity, are perhaps more closely representative of variations in patient populations and may improve translation to the clinic.

In conclusion, C.*mdx*62 mice represent the first dystrophin deficient murine model on a pure BALB/c background with an 8 bp deletion in exon 62, that exhibit a dystrophic pathology in limb muscles and diaphragm and a bone phenotype, up to 12 months of age. While continued studies into the pathology and mechanisms underlying dystrophic progression will prove valuable in understanding this model, the variation in background strain and mutation location makes the C.*mdx*62 mouse an important addition to the preclinical toolbox for DMD research.

Materials and methods

Experimental animals

All experiments were approved by the Animal Ethics Committee of The University of Melbourne and conducted in accordance with the Australian code for the care and use of animals for scientific purposes as stipulated by the National Health and Medical Research Council (Australia). Male BALB/c WT mice were obtained from the Animal Resources Centre (Canning Vale, Western Australia) and BALB/c C.*mdx*62 mice were bred in the Biological Research Facility at The University of Melbourne. All mice were housed in the Biological Research Facility under a 12:12-hour light-dark cycle, with water and standard laboratory chow available *ad libitum*.

CRISPR-mediated mutagenesis of dystrophin

C.*mdx*62 mice were created in collaboration with the MAGEC facility at The Walter and Eliza Hall Institute (Melbourne, Australia). To generate mice, 20 ng/µl of Cas9 mRNA, 10 ng/µl of sgRNA (GGGCACTTTGTTTGGTGAGA) and 40 ng/µl of oligo donor (tttcttttctttttcctttttttctttttgcagCTTCAGTTCAGGGTCCCTGGGAGAGAGCtATCGAGCCAA ACAAAGTGCCCTACTATATCAAgtaagtcaaaagcatttatgtacctgatctgtat) were injected into the cytoplasm of fertilized one-cell stage embryos derived from WT BALB/c breeders. Viable founder mice were identified by next-generation sequencing. Targeted animals were backcrossed onto BALB/c mice for two generations to eliminate potential sgRNA off-target hits. Founder mice were backcrossed to WT BALB/c mice for two generations and tail snips were genotyped through Transnetyx (Transnetyx, Cordova, TN, USA) to identify the presence or absence of the 8 bp deletion. Once backcrossed, mice were interbred to generate a homozygous colony. These mice have been cryopreserved and are available for use via the Australian Phenome Bank (strain ID: 9150; Home - Australian Phenomics Facility (apf.edu.au)).

Muscle function

At 3, 6, or 12 months of age, mice were anesthetized with sodium pentobarbital (Nembutal; 60 mg/kg, Sigma-Aldrich, Castle Hill, N.S.W., Australia) via intraperitoneal injection and contractile properties of the tibialis anterior (TA) muscles assessed *in situ* with an intact nerve

and blood supply, as described previously (Gehrig et al., 2010, Hardee et al., 2021, Lynch, 2004). This included assessments of isometric twitch and tetanic contractile characteristics and the frequency-force relationship, as outlined in the TREAT-NMD SOP (DMD_M.2.2.005), followed by an assessment of the muscle susceptibility to contraction-mediated injury, based on the cumulative deficit in isometric force production after repeated lengthening contractions. Isolated muscles were maximally activated to produce isometric force and then stretched to perform an eccentric contraction (at a velocity of 2 L_f/s) at progressively increasing magnitudes of stretch. Maximum isometric force was determined before each eccentric contraction. The muscles were set at an increasing resting length to a maximum of 30% of L_f and stimulated at at 120 Hz. At the conclusion of these measurements, the muscles of the left hindlimb (including the TA, extensor digitorum longus (EDL), soleus and quadriceps) as well as the epididymal fat, spleen, liver, diaphragm and heart, were excised, trimmed of tendon and any non-muscle tissue, blotted once on filter paper, and weighed on an analytical balance. The EDL, soleus, quadriceps, epididymal fat, liver, and a piece of diaphragm muscle were snap frozen for later analyses. The TA and a second piece of diaphragm muscle were mounted in optimal cutting temperature (OCT) compound and frozen in thawing isopentane for later histochemical analyses. Mice were killed as a consequence of diaphragm and heart excision while they were anesthetized deeply.

Serum analysis

Whole blood was collected from mice (n=5-9/group) into Eppendorf tubes at endpoint via cardiac puncture. To isolate serum, tubes were left incubated for 30 min at room temperature for 30 min, then centrifuged 5000 g for 10 min at 4°C and serum removed to fresh Eppendorf tubes and stored at -80°C. As serum creatine kinase (CK) levels from dystrophic mice are in the range of 1339-55620 U/L, with a mean of 18532 ± 14577 (TREAT-NMD Activity A07: Accelerate preclinical phase of new therapeutic treatment development), which is outside the measurable range of the Equine Profile Plus rotor (0-14,000 U/L), it was not possible to accurately assess these levels in the C.*mdx*62 mouse. Therefore, levels of serum aspartate aminotransferase (AST) were used as a biomarker of DMD muscle pathology and measured on a VetScan VS2 chemistry analyzer (Abaxis Inc., Union City, CA, USA) using the Equine Profile Plus rotor according to the manufacturer's protocol.

Western immunoblotting

For protein analyses, tissues were homogenized in ice-cold buffer (10 mM Tris-HCl (pH 7.4), 100 mM NaCl, 1 mM EDTA, 1 mM EGTA, 1 mM NaF, 1% Triton, 10% glycerol, 0.1% SDS, 20 mM $Na4P_2O_7$, 0.5 mM Na_3VO_4, 0.5% sodium deoxycholate, 0.1 mM PMSF and protease and phosphatase inhibitors (all from Sigma-Aldrich, St. Louis, MO, USA). Samples were centrifuged at 10,000 g for 5 min at 4°C and the resulting supernatant analyzed for total protein content (DC Protein Assay; Bio-Rad Laboratories, Hercules, CA, USA), with BSA standards. Samples were normalized to 2 µg/µL in homogenizing buffer containing 4× Laemmeli sample buffer [0.25M Tris-HCl, pH 6.8, 6% SDS, 40% glycerol, 0.04% bromophenol blue, 16% DTT], and heated for 3 min at 95°C. Lysates were run on run on 4-15% Criterion TGX Stain-Free gels (Bio-Rad Laboratories, Gladesville, NSW, Australia) at a constant voltage of 100 V and transferred to PVDF membranes. Membranes were blocked for 1 h at room temperature (RT) in Tris-buffered saline-Tween 20 (TBST) containing 5% BSA and incubated with primary antibodies diluted in 5% BSA/TBST overnight at 4°C, including mouse-α-dystrophin MANEX1011B(1C7) (1:1000; deposited by Morris, G.E; Developmental Studies Hybridoma Bank, The University of Iowa; USA), mouse-α-β-dystroglycan (1:500; B-DG-CE; Leica Biosystems), mouse-α-utrophin (1:1000; #610896; BD Biosciences), mouse-α-dystrophin MANDRA 7A10 (1:1000; #D8043; Sigma Aldrich), rabbit-α-phospholamban (Ser16; #7052; 1:1000; Merck Millipore) and goat-anti-total phospholamban (1:1000; #sc21923; Santa Cruz Biotechnologies). The following day, membranes were washed in TBST and incubated for 1 h at RT in horseradish peroxidase (HRP)-conjugated sheep-α-mouse IgG (#NA931; Cytiva Life Sciences, Sao Paulo, SP), donkey-α-goat (#ab97110; Abcam), or donkey-α-rabbit IgG (#NA934V; Cytiva Life Sciences) at 1:5000 in 5% BSA/TBST. After washing in TBST, membranes were treated with enhanced chemiluminescence (Immobilon Forte Western HRP substrate; EMD Millipore Corp, Hayward, CA, USA). Samples were evaluated by integrated densitometry using a ChemiDoc XRS machine and Image Lab software (Bio-Rad Laboratories, Hercules, CA, USA). To confirm equal loading between lanes, stain free blots were imaged on the ChemiDoc, according to manufacturer's instructions.

Histology

Serial sections (8 μm) of TA or diaphragm muscles were cut transversely using a refrigerated (-20°C) cryostat (CTI Cryostat; IEC, Needham Heights, MA) and stained with hematoxylin and eosin to assess overall muscle structure, or Van Gieson's to determine collagen infiltration as an indicator of fibrosis, as described previously (Gehrig et al., 2010). Digital images of stained sections were obtained using an upright microscope with camera (Axio Imager, Carl Zeiss, Wrek, Göttingen, Germany), controlled by AxioVision AC software (AxioVision AC Rel. 4.8, Carl Zeiss Imaging Solutions, Wrek, Göttingen, Germany). Images were quantified for fibrosis content using FIJI/ImageJ software (Fiji v2.5.0, Fiji (imagej.net)).

Immunofluorescence

For assessment of muscle fiber type and oxidative capacity, transverse serial sections (8 μm) were stained with SC-71 and BF-F3 (both developed by S. Schiaffino, University of Padova (Padua, Italy) (obtained from the Developmental Studies Hybridoma Bank), and reacted with SDH, as described previously (Murphy et al., 2019). For detection of syntrophin and sarcoglycan, frozen sections were thawed at RT and incubated 1 h RT in either Ms-α-α-sarcoglycan (NCL-L-a-SARC, Leica biosystems) or Ms-α-syntrophin (SAB4200213, Sigma Aldrich) at 1:100 dilution in 10% normal goat serum in TBS. Sections were rinsed in TBS 2 × 5 min, incubated 1 h RT in AF647-conjugated Gt-α-Ms IgG1 secondary antibody (A21240, Invitrogen) at 1:400 dilution in 10% normal goat serum in TBS, incubated with DAPI (1:1000 in TBS) for 10 min at RT, rinsed in TBS 2 × 5min, then dipped in PBS.

For detection of utrophin and the acetylcholine receptor (AChR), sections were fixed in ice cold acetone for 2 min at RT, rinsed in PBS (3×), then blocked in 5% normal goat serum/1% BSA for 1 h at RT. Sections were incubated at 4˚C in Ms-α-utrophin (sc-33700, Santa Cruz Technologies) 1:50 and Ms-α-AChR (#610989, BD Biosciences) 1:50 in 1% BSA/PBS. The next day, sections were rinsed in 0.1% Triton/PBS 3 × 5 min, incubated with AF647-conjugated Gt-anti-Ms IgG1 (A21240, Invitrogen) + AF488-conjugated Gt-anti-Ms IgG2a (A21131, Invitrogen) 1:400 in 1% BSA/PBS for 1 h at RT, stained with DAPI (1:5000 in 0.1% Triton/PBS) for 10 min at RT, and rinsed in 0.1% Triton/PBS for 3 × 5 min.

For detection of dystrophin and β-dystroglycan, sections were fixed in 4% paraformaldehyde for 15 min at RT, rinsed in in 0.1% Triton/PBS for 2 × 5 min, then subject to heat-activated antigen retrieval in citrate buffer (pH 6.0, Sigma Aldrich) in a pressure cooker for 10 min.

Once cooled, sections were rinsed in 0.1% in 0.1% Triton/PBS for 2 × 5 min, blocked in 10% normal goat serum/3% BSA for 45 min at RT, and incubated at 4˚C in Ms-α-dystrophin MANDRA1 7A10 (sc-47760, Santa Cruz Technologies) 1:100 and Ms-α-β-dystroglycan (NCL-bDG, Leica Biosystems) 1:50 in 3% BSA in 0.1% Triton/PBS. The next day, sections were rinsed in 0.1% PBS/Tween-20 3 × 10 min, incubated with AF647-conjgated Gt-α-mouse IgG1 (A21240, Invitrogen, 1:200) and AF555-conjugated Gt-α-mouse IgG2a (A21137, Invitrogen, 1:400) in 3% BSA/TBST for 1 h at RT, stained with DAPI (1:5000 in 0.1% in 0.1% Triton/PBS) for 10 min at RT, and rinsed with 0.1% in 0.1% Triton/PBS for 3 × 10 min.

For detection of laminin and IgG, sections were fixed in 4% paraformaldehyde for 10 min at RT, rinsed in PBS, washed in 0.1% Triton/PBS (2× 5 min), blocked in 10% normal goat serum in 2% BSA/PBST 1 h at RT, and incubated 1 h RT in Rb-α-laminin antibody (#L9393, Sigma Aldrich) at 1:25 dilution in 2% BSA/ in 0.1% Triton/PBS. Sections were washed 3 × 5 min with 0.1% Triton/PBS then incubated 2 h RT in AF555-conjugated Gt-α-Rb IgG (A21428, Invitrogen) and AF488-conjugated Gt-α-Ms IgG (H+L, A11029, Invitrogen) secondary antibodies at 1:250 dilution in 2% BSA in 0.1% Triton/PBS. Sections were incubated with DAPI (1:5000 in in 0.1% Triton/PBS) for 10 min at RT and rinsed in 0.1% in 0.1% Triton/PBS 3 × 5min.

At the conclusion of staining, all sections were air dried and mounted with glass coverslips using Mowiol, then allowed to dry overnight prior to imaging. Digital images of stained sections were obtained using an upright microscope with camera (Axio Imager, Carl Zeiss, Wrek, Göttingen, Germany), controlled by AxioVision AC software (AxioVision AC Rel. 4.8, Carl Zeiss Imaging Solutions, Wrek, Göttingen, Germany). Images were quantified for muscle fiber size, percentage of central nuclei, or percent of IgG positive muscle fibers using FIJI/ImageJ software (Fiji v2.5.0, Fiji (imagej.net)).

qPCR

Total RNA was extracted from the heart (n=5-9/genotype/timepoint) using TRIzol/chloroform followed by the RNeasy Fibrous Tissue Mini Kit (Qiagen) as per manufacturer's instructions. The concentration and quality of RNA samples was determined using a Nanodrop 2000 spectrophotometer (Thermo Scientific, Waltham, MA, USA). Real-time RT-PCR was performed as described previously (Murphy et al., 2019, Swiderski et al., 2016) using the following forward and reverse primer sequences: F4/80, 5'-

CATCAGCCATGTGGGTACAG-3' and 5'-CATCACTGCCTCCACTAGCA-3'; TGFβ, 5'-TGAGTGGCTGTCTTTTGACG-3' and 5'-TCTCTGTGGAGCTGAAGCAA-3'; Col1a1, 5'-CACCCTCAAGAGCCTGAGTC-3' and 5'-GTTCGGGCTGATGTACCAGT-3'; Col3a1, 5'-ACCAAAAGGTGATGCTGGAC-3' and 5'-GACCTCGTGCTCCAGTTAGC-3'; Col6a1, 5'-CCCCATTGGACCTAAAGGAT-3' and 5'-TCTCCCACTTCACCCTCATC-3'; Runx2, 5'-GCCTTCAAGGTTGTAGCCCT-3' and 5'- GTTCTCATCATTCCCGGCCA-3'; Osx, 5'- GTCCTCTCTGCTTGAGGAAGAA-3' and 5'-GGGCTGAAAGGTCAGCGTAT-3'; Ocn, 5'- TTCTGCTCACTCTGCTGACC-3' and 5'-GGGACTGAGGCTCCAAGGTA-3'; Alp, 5'-CAGGCCGCCTTCATAAGCA-3' and 5'-AATTGACGTTCCGATCCTGC-3'. Gene expression was quantified using a cycle threshold (C_T) method. Relative gene expression was calculated using the expression $2^{-\Delta CT}$, normalized to total cDNA content as determined using the Quant-iT™ OliGreen™ ssDNA assay kit and Quant-iT OliGreen ssDNA reagent (Thermo Scientific).

Micro-computed tomographic (micro-CT) scanning and analysis

Tibiae were carefully excised and fixed in 4% paraformaldehyde for 24 h, rinsed in PBS and stored in PBS. Tibiae were scanned using the Skyscan 1276 (Bruker micro-CT) at 9 µm resolution, 0.25 mm aluminium filter, 56 kV voltage, 200 µA, 560 ms exposure time, 0.4° step rotation with frame averaging of 2. Images were reconstructed and analyzed using NRecon (v1.7.4.6), Dataviewer (v1.5.6.2), CT Analyzer (CTAn; v1.18.8.0) and CTVox (v3.3.0 r1403). Tibial lengths were determined after scanning. Regions of interest (ROIs) were determined as described previously (Chan et al., 2021). Trabecular bone was assessed in the proximal region commencing at 3% of bone length from the growth plate and extended distally for a total of 13.5% (equivalent to 0.5-3 mm of the growth plate). For cortical bone, a region of interest beginning at 50% of bone length and extending distally for 2% (approximately 0.5 mm) was used for 3D cortical bone analyses using CT Analyzer. Representative images were taken at the mid-diaphysis (50% of bone length) using a pseudodensity filter in CTVox.

The length of the tibial crest was measured using a custom script written in FIJI (ImageJ) using individual cross-sectional images spanning 15% to 40% of the tibial length, as described previously (Chan et al., 2023).

Statistics

Data were analyzed between groups using either a Student's t-test or a two-way ANOVA, where appropriate, with Bonferonni's post-hoc multiple comparisons test used to detect significant differences between means. Where data were determined to be not normally distributed, a Mann-Whitney U test was used. A P value less than 0.05 was considered statistically significant. All statistical analyses were carried out using Prism GraphPad 6 software (GraphPad Software Inc., La Jolla, CA, USA). All values are presented as mean ± standard error of mean (SEM).

Acknowledgments

The author/s acknowledge the facilities, and the scientific and technical assistance of The Melbourne Advanced Genome Editing Centre (MAGEC). MAGEC is supported by Phenomics Australia (PA). PA is supported by the Australian Government through the National Collaborative Research Infrastructure Strategy (NCRIS) program. These studies had their origins from related research supported by the National Health and Medical Research Council of Australia (GRNT1144772).

Conflict of Interest Statement

The authors declare they have no conflict of interest.

Author contributions

Conceptualization: K.S., P.G., G.S.L.; Methodology: A.K., M.H.; Investigation: K.S., A.S.C., J.D.C., J.P.H., J.T., A.C., T.N.; Formal analysis: K.S., A.S.C., P.G., G.S.L.; Writing – original draft preparation: K.S., A.S.C., P.G., G.S.L.; Writing – review and editing: K.S., A.S.C., P.G., G.S.L. Supervision: P.G., G.S.L; Project administration: K.S., P.G., G.S.L.; Funding acquisition: K.S., P.G., G.S.L. All authors had the opportunity to comment on the manuscript.

References

ACHARYYA, S., BUTCHBACH, M. E., SAHENK, Z., WANG, H., SAJI, M., CARATHERS, M., RINGEL, M. D., SKIPWORTH, R. J., FEARON, K. C., HOLLINGSWORTH, M. A., MUSCARELLA, P., BURGHES, A. H., RAFAEL-FORTNEY, J. A. & GUTTRIDGE, D. C. 2005. Dystrophin glycoprotein complex dysfunction: a regulatory link between muscular dystrophy and cancer cachexia. *Cancer Cell,* 8**,** 421-32.

AMOASII, L., LONG, C., LI, H., MIREAULT, A. A., SHELTON, J. M., SANCHEZ-ORTIZ, E., MCANALLY, J. R., BHATTACHARYYA, S., SCHMIDT, F., GRIMM, D., HAUSCHKA, S. D., BASSEL-DUBY, R. & OLSON, E. N. 2017. Single-cut genome editing restores dystrophin expression in a new mouse model of muscular dystrophy. *Sci Transl Med,* 9.

ANDERSON, J. E., LENTZ, D. L. & JOHNSON, R. B. 1993. Recovery from disuse osteopenia coincident to restoration of muscle strength in mdx mice. *Bone,* 14**,** 625-34.

ARAKI, E., NAKAMURA, K., NAKAO, K., KAMEYA, S., KOBAYASHI, O., NONAKA, I., KOBAYASHI, T. & KATSUKI, M. 1997. Targeted disruption of exon 52 in the mouse dystrophin gene induced muscle degeneration similar to that observed in Duchenne muscular dystrophy. *Biochem Biophys Res Commun,* 238**,** 492-7.

BARBONI, M. T. S., LIBER, A. M. P., JOACHIMSTHALER, A., SAOUDI, A., GOYENVALLE, A., RENDON, A., ROGER, J. E., VENTURA, D. F., KREMERS, J. & VAILLEND, C. 2021. Altered visual processing in the mdx52 mouse model of Duchenne muscular dystrophy. *Neurobiol Dis,* 152**,** 105288.

BARTON-DAVIS, E. R., CORDIER, L., SHOTURMA, D. I., LELAND, S. E. & SWEENEY, H. L. 1999. Aminoglycoside antibiotics restore dystrophin function to skeletal muscles of mdx mice. *J Clin Invest,* 104**,** 375-81.

BITETTI, I., MAUTONE, C., BERTELLA, M., MANNA, M. R. & VARONE, A. 2021. Early treatment with Ataluren of a 2-year-old boy with nonsense mutation Duchenne dystrophy. *Acta Myol,* 40**,** 184-186.

BLANKINSHIP, M. J., GREGOREVIC, P. & CHAMBERLAIN, J. S. 2006. Gene therapy strategies for Duchenne muscular dystrophy utilizing recombinant adeno-associated virus vectors. *Mol Ther,* 13**,** 241-9.

BOSTICK, B., SHIN, J. H., YUE, Y., WASALA, N. B., LAI, Y. & DUAN, D. 2012. AAV micro-dystrophin gene therapy alleviates stress-induced cardiac death but not myocardial fibrosis in >21-m-old mdx mice, an end-stage model of Duchenne muscular dystrophy cardiomyopathy. *J Mol Cell Cardiol,* 53**,** 217-22.

BUSHBY, K., FINKEL, R., BIRNKRANT, D. J., CASE, L. E., CLEMENS, P. R., CRIPE, L., KAUL, A., KINNETT, K., MCDONALD, C., PANDYA, S., POYSKY, J., SHAPIRO, F., TOMEZSKO, J., CONSTANTIN, C. & GROUP, D. M. D. C. C. W. 2010. Diagnosis and management of Duchenne muscular dystrophy, part 1: diagnosis, and pharmacological and psychosocial management. *Lancet Neurol,* 9**,** 77-93.

CHADWICK, K. P., MUESKE, N. M., HORENSTEIN, R. E., SHEFELBINE, S. J. & WREN, T. A. L. 2018. Children with myelomeningocele do not exhibit normal remodeling of tibia roundness with physical development. *Bone,* 114**,** 292-297.

CHAN, A. S., HARDEE, J. P., BLANK, M., CHO, E. H., MCGREGOR, N. E., SIMS, N. A. & LYNCH, G. S. 2023. Increasing muscle contractility through low-frequency stimulation alters tibial bone geometry and reduces bone strength in mdx and dko dystrophic mice. *J Appl Physiol (1985),* 135**,** 77-87.

CHAN, A. S. M., MCGREGOR, N. E., POULTON, I. J., HARDEE, J. P., CHO, E. H., MARTIN, T. J., GREGOREVIC, P., SIMS, N. A. & LYNCH, G. S. 2021. Bone Geometry Is Altered by Follistatin-Induced Muscle Growth in Young Adult Male Mice. *JBMR Plus,* 5**,** e10477.

CHEMELLO, F., WANG, Z., LI, H., MCANALLY, J. R., LIU, N., BASSEL-DUBY, R. & OLSON, E. N. 2020. Degenerative and regenerative pathways underlying Duchenne muscular dystrophy revealed by single-nucleus RNA sequencing. *Proc Natl Acad Sci U S A,* 117**,** 29691-29701.

COLEY, W. D., BOGDANIK, L., VILA, M. C., YU, Q., VAN DER MEULEN, J. H., RAYAVARAPU, S., NOVAK, J. S., NEARING, M., QUINN, J. L., SAUNDERS, A., DOLAN, C., ANDREWS, W., LAMMERT, C., AUSTIN, A., PARTRIDGE, T. A., COX, G. A., LUTZ, C. & NAGARAJU, K. 2016. Effect of genetic background on the dystrophic phenotype in mdx mice. *Hum Mol Genet,* 25**,** 130-45.

COX, G. A., PHELPS, S. F., CHAPMAN, V. M. & CHAMBERLAIN, J. S. 1993. New mdx mutation disrupts expression of muscle and nonmuscle isoforms of dystrophin. *Nat Genet,* 4**,** 87-93.

DECONINCK, A. E., RAFAEL, J. A., SKINNER, J. A., BROWN, S. C., POTTER, A. C., METZINGER, L., WATT, D. J., DICKSON, J. G., TINSLEY, J. M. & DAVIES, K. E. 1997. Utrophin-dystrophin-deficient mice as a model for Duchenne muscular dystrophy. *Cell,* 90**,** 717-27.

DECONINCK, N., RAFAEL, J. A., BECKERS-BLEUKX, G., KAHN, D., DECONINCK, A. E., DAVIES, K. E. & GILLIS, J. M. 1998. Consequences of the combined deficiency in dystrophin and utrophin on the mechanical properties and myosin composition of some limb and respiratory muscles of the mouse. *Neuromuscul Disord,* 8**,** 362-70.

DUAN, D. 2018. Systemic AAV Micro-dystrophin Gene Therapy for Duchenne Muscular Dystrophy. *Mol Ther,* 26**,** 2337-2356.

DUAN, D., GOEMANS, N., TAKEDA, S., MERCURI, E. & AARTSMA-RUS, A. 2021. Duchenne muscular dystrophy. *Nat Rev Dis Primers,* 7**,** 13.

DUDDY, W., DUGUEZ, S., JOHNSTON, H., COHEN, T. V., PHADKE, A., GORDISH-DRESSMAN, H., NAGARAJU, K., GNOCCHI, V., LOW, S. & PARTRIDGE, T. 2015. Muscular dystrophy in the mdx mouse is a severe myopathy compounded by hypotrophy, hypertrophy and hyperplasia. *Skelet Muscle,* 5**,** 16.

DUNANT, P., WALTER, M. C., KARPATI, G. & LOCHMULLER, H. 2003. Gentamicin fails to increase dystrophin expression in dystrophin-deficient muscle. *Muscle Nerve,* 27**,** 624-7.

EATON, G. J., CUSTER, R. P., JOHNSON, F. N. & STABENOW, K. T. 1978. Dystrophic cardiac calcinosis in mice: genetic, hormonal, and dietary influences. *Am J Pathol,* 90**,** 173-86.

ERVASTI, J. M. & CAMPBELL, K. P. 1993. A role for the dystrophin-glycoprotein complex as a transmembrane linker between laminin and actin. *J Cell Biol,* 122**,** 809-23.

FABB, S. A., WELLS, D. J., SERPENTE, P. & DICKSON, G. 2002. Adeno-associated virus vector gene transfer and sarcolemmal expression of a 144 kDa micro-dystrophin effectively restores the dystrophin-associated protein complex and inhibits myofibre degeneration in nude/mdx mice. *Hum Mol Genet,* 11**,** 733-41.

GARBINCIUS, J. F. & MICHELE, D. E. 2015. Dystrophin-glycoprotein complex regulates muscle nitric oxide production through mechanoregulation of AMPK signaling. *Proc Natl Acad Sci U S A,* 112**,** 13663-8.

GEHRIG, S. M., KOOPMAN, R., NAIM, T., TJOAKARFA, C. & LYNCH, G. S. 2010. Making fast-twitch dystrophic muscles bigger protects them from contraction injury and attenuates the dystrophic pathology. *Am J Pathol,* 176**,** 29-33.

GLASS, A. M., COOMBS, W. & TAFFET, S. M. 2013. Spontaneous cardiac calcinosis in BALB/cByJ mice. *Comp Med,* 63**,** 29-37.

GREGOREVIC, P., BLANKINSHIP, M. J., ALLEN, J. M., CRAWFORD, R. W., MEUSE, L., MILLER, D. G., RUSSELL, D. W. & CHAMBERLAIN, J. S. 2004. Systemic delivery of genes to striated muscles using adeno-associated viral vectors. *Nat Med,* 10**,** 828-34.

GROUNDS, M. D. & LLOYD, E. M. 2023. Considering the Promise of Vamorolone for Treating Duchenne Muscular Dystrophy. *J Neuromuscul Dis,* 10**,** 1013-1030.

HAM, D. J., GARDNER, A., KENNEDY, T. L., TRIEU, J., NAIM, T., CHEE, A., ALVES, F. M., CALDOW, M. K., LYNCH, G. S. & KOOPMAN, R. 2019. Glycine administration attenuates progression of dystrophic pathology in prednisolone-treated dystrophin/utrophin null mice. *Sci Rep,* 9**,** 12982.

HAMMERS, D. W., HART, C. C., MATHENY, M. K., WRIGHT, L. A., ARMELLINI, M., BARTON, E. R. & SWEENEY, H. L. 2020. The D2.mdx mouse as a preclinical model of the skeletal muscle pathology associated with Duchenne muscular dystrophy. *Sci Rep,* 10**,** 14070.

HAMRICK, M. W., MCPHERRON, A. C. & LOVEJOY, C. O. 2002. Bone mineral content and density in the humerus of adult myostatin-deficient mice. *Calcif Tissue Int,* 71**,** 63-8.

HAMRICK, M. W., MCPHERRON, A. C., LOVEJOY, C. O. & HUDSON, J. 2000. Femoral morphology and cross-sectional geometry of adult myostatin-deficient mice. *Bone,* 27**,** 343-9.

HARDEE, J. P., MARTINS, K. J. B., MIOTTO, P. M., RYALL, J. G., GEHRIG, S. M., RELJIC, B., NAIM, T., CHUNG, J. D., TRIEU, J., SWIDERSKI, K., PHILP, A. M., PHILP, A., WATT, M. J., STROUD, D. A., KOOPMAN, R., STEINBERG, G. R. & LYNCH, G. S. 2021. Metabolic remodeling of dystrophic skeletal muscle reveals biological roles for dystrophin and utrophin in adaptation and plasticity. *Mol Metab,* 45**,** 101157.

HOFFMAN, E. P. 2020. The discovery of dystrophin, the protein product of the Duchenne muscular dystrophy gene. *FEBS J,* 287**,** 3879-3887.

HOFFMAN, E. P., BROWN, R. H., JR. & KUNKEL, L. M. 1987. Dystrophin: the protein product of the Duchenne muscular dystrophy locus. *Cell,* 51**,** 919-28.

HUGNOT, J. P., GILGENKRANTZ, H., VINCENT, N., CHAFEY, P., MORRIS, G. E., MONACO, A. P., BERWALD-NETTER, Y., KOULAKOFF, A., KAPLAN, J. C., KAHN, A. & ET AL. 1992. Distal transcript of the dystrophin gene initiated from an alternative first exon and encoding a 75-kDa protein widely distributed in nonmuscle tissues. *Proc Natl Acad Sci U S A,* 89**,** 7506-10.

KENJO, E., HOZUMI, H., MAKITA, Y., IWABUCHI, K. A., FUJIMOTO, N., MATSUMOTO, S., KIMURA, M., AMANO, Y., IFUKU, M., NAOE, Y., INUKAI, N. & HOTTA, A. 2021. Low immunogenicity of LNP allows repeated administrations of CRISPR-Cas9 mRNA into skeletal muscle in mice. *Nat Commun,* 12**,** 7101.

KENNEDY, T. L., GUIRAUD, S., EDWARDS, B., SQUIRE, S., MOIR, L., BABBS, A., ODOM, G., GOLEBIOWSKI, D., SCHNEIDER, J., CHAMBERLAIN, J. S. & DAVIES, K. E. 2018. Micro-utrophin Improves Cardiac and Skeletal Muscle Function of Severely Affected D2/mdx Mice. *Mol Ther Methods Clin Dev,* 11**,** 92-105.

KENNEDY, T. L., SWIDERSKI, K., MURPHY, K. T., GEHRIG, S. M., CURL, C. L., CHANDRAMOULI, C., FEBBRAIO, M. A., DELBRIDGE, L. M., KOOPMAN, R. & LYNCH, G. S. 2016. BGP-15 Improves Aspects of the Dystrophic Pathology in mdx and dko Mice with Differing Efficacies in Heart and Skeletal Muscle. *Am J Pathol,* 186**,** 3246-3260.

KIM, K., RYU, S. M., KIM, S. T., BAEK, G., KIM, D., LIM, K., CHUNG, E., KIM, S. & KIM, J. S. 2017. Highly efficient RNA-guided base editing in mouse embryos. *Nat Biotechnol,* 35**,** 435-437.

KING, W. M., RUTTENCUTTER, R., NAGARAJA, H. N., MATKOVIC, V., LANDOLL, J., HOYLE, C., MENDELL, J. R. & KISSEL, J. T. 2007. Orthopedic outcomes of long-term daily corticosteroid treatment in Duchenne muscular dystrophy. *Neurology,* 68**,** 1607-13.

KOO, T., LU-NGUYEN, N. B., MALERBA, A., KIM, E., KIM, D., CAPPELLARI, O., CHO, H. Y., DICKSON, G., POPPLEWELL, L. & KIM, J. S. 2018. Functional Rescue of Dystrophin Deficiency in Mice Caused by Frameshift Mutations Using Campylobacter jejuni Cas9. *Mol Ther,* 26**,** 1529-1538.

LANGENBACH, K. J. & RANDO, T. A. 2002. Inhibition of dystroglycan binding to laminin disrupts the PI3K/AKT pathway and survival signaling in muscle cells. *Muscle Nerve,* 26**,** 644-53.

LARSON, C. M. & HENDERSON, R. C. 2000. Bone mineral density and fractures in boys with Duchenne muscular dystrophy. *J Pediatr Orthop,* 20**,** 71-4.

LEDERFEIN, D., YAFFE, D. & NUDEL, U. 1993. A housekeeping type promoter, located in the 3' region of the Duchenne muscular dystrophy gene, controls the expression of Dp71, a major product of the gene. *Hum Mol Genet,* 2**,** 1883-8.

LIU, M., YUE, Y., HARPER, S. Q., GRANGE, R. W., CHAMBERLAIN, J. S. & DUAN, D. 2005. Adeno-associated virus-mediated microdystrophin expression protects young mdx muscle from contraction-induced injury. *Mol Ther,* 11**,** 245-56.

LU, Q. L., MANN, C. J., LOU, F., BOU-GHARIOS, G., MORRIS, G. E., XUE, S. A., FLETCHER, S., PARTRIDGE, T. A. & WILTON, S. D. 2003. Functional amounts of dystrophin produced by skipping the mutated exon in the mdx dystrophic mouse. *Nat Med,* 9**,** 1009-14.

LYNCH, G. S. 2004. Role of contraction-induced injury in the mechanisms of muscle damage in muscular dystrophy. *Clin Exp Pharmacol Physiol,* 31**,** 557-61.

LYNCH, G. S., HINKLE, R. T., CHAMBERLAIN, J. S., BROOKS, S. V. & FAULKNER, J. A. 2001. Force and power output of fast and slow skeletal muscles from mdx mice 6-28 months old. *J Physiol,* 535**,** 591-600.

MAINO, E., WOJTAL, D., EVAGELOU, S. L., FARHEEN, A., WONG, T. W. Y., LINDSAY, K., SCOTT, O., RIZVI, S. Z., HYATT, E., ROK, M., VISUVANATHAN, S., CHIODO, A., SCHNEEWEISS, M., IVAKINE, E. A. & COHN, R. D. 2021. Targeted genome editing in vivo corrects a Dmd duplication restoring wild-type dystrophin expression. *EMBO Mol Med,* 13**,** e13228.

MALIK, V., RODINO-KLAPAC, L. R., VIOLLET, L., WALL, C., KING, W., AL-DAHHAK, R., LEWIS, S., SHILLING, C. J., KOTA, J., SERRANO-MUNUERA, C., HAYES, J., MAHAN, J. D., CAMPBELL, K. J., BANWELL, B., DASOUKI, M., WATTS, V., SIVAKUMAR, K., BIEN-WILLNER, R., FLANIGAN, K. M., SAHENK, Z., BAROHN, R. J., WALKER, C. M. & MENDELL, J. R. 2010. Gentamicin-induced readthrough of stop codons in Duchenne muscular dystrophy. *Ann Neurol,* 67**,** 771-80.

MAZALA, D. A., NOVAK, J. S., HOGARTH, M. W., NEARING, M., ADUSUMALLI, P., TULLY, C. B., HABIB, N. F., GORDISH-DRESSMAN, H., CHEN, Y. W., JAISWAL, J. K. & PARTRIDGE, T. A. 2020. TGF-beta-driven muscle degeneration and failed regeneration underlie disease onset in a DMD mouse model. *JCI Insight,* 5.

MCDONALD, D. G., KINALI, M., GALLAGHER, A. C., MERCURI, E., MUNTONI, F., ROPER, H., JARDINE, P., JONES, D. H. & PIKE, M. G. 2002. Fracture prevalence in Duchenne muscular dystrophy. *Dev Med Child Neurol,* 44**,** 695-8.

MERCURI, E., BONNEMANN, C. G. & MUNTONI, F. 2019. Muscular dystrophies. *Lancet,* 394**,** 2025-2038.

MERCURI, E., MUNTONI, F., OSORIO, A. N., TULINIUS, M., BUCCELLA, F., MORGENROTH, L. P., GORDISH-DRESSMAN, H., JIANG, J., TRIFILLIS, P., ZHU, J., KRISTENSEN, A., SANTOS, C. L., HENRICSON, E. K., MCDONALD, C. M., DESGUERRE, I., STRIDE & INVESTIGATORS, C. D. N. H. 2020. Safety and effectiveness of ataluren: comparison of results from the STRIDE Registry and CINRG DMD Natural History Study. *J Comp Eff Res,* 9**,** 341-360.

MICHOROWSKA, S. 2021. Ataluren-Promising Therapeutic Premature Termination Codon Readthrough Frontrunner. *Pharmaceuticals (Basel),* 14.

MIN, Y. L., CHEMELLO, F., LI, H., RODRIGUEZ-CAYCEDO, C., SANCHEZ-ORTIZ, E., MIREAULT, A. A., MCANALLY, J. R., SHELTON, J. M., ZHANG, Y., BASSEL-DUBY, R. & OLSON, E. N. 2020. Correction of Three Prominent Mutations in Mouse and Human Models of Duchenne Muscular Dystrophy by Single-Cut Genome Editing. *Mol Ther,* 28**,** 2044-2055.

MIN, Y. L., LI, H., RODRIGUEZ-CAYCEDO, C., MIREAULT, A. A., HUANG, J., SHELTON, J. M., MCANALLY, J. R., AMOASII, L., MAMMEN, P. P. A., BASSEL-DUBY, R. & OLSON, E. N. 2019. CRISPR-Cas9 corrects Duchenne muscular dystrophy exon 44 deletion mutations in mice and human cells. *Sci Adv,* 5**,** eaav4324.

MODLESKY, C. M., KANOFF, S. A., JOHNSON, D. L., SUBRAMANIAN, P. & MILLER, F. 2009. Evaluation of the femoral midshaft in children with cerebral palsy using magnetic resonance imaging. *Osteoporos Int,* 20**,** 609-15.

MONTGOMERY, E., PENNINGTON, C., ISALES, C. M. & HAMRICK, M. W. 2005. Muscle-bone interactions in dystrophin-deficient and myostatin-deficient mice. *Anat Rec A Discov Mol Cell Evol Biol,* 286**,** 814-22.

MURPHY, K. T., HOSSAIN, M. I., SWIDERSKI, K., CHEE, A., NAIM, T., TRIEU, J., HAYNES, V., READ, S. J., STAPLETON, D. I., JUDGE, S. M., TREVINO, J. G., JUDGE, A. R. & LYNCH, G. S. 2019. Mas Receptor Activation Slows Tumor Growth and Attenuates Muscle Wasting in Cancer. *Cancer Res,* 79**,** 706-719.

NAKAGAKI, W. R., BERTRAN, C. A., MATSUMURA, C. Y., SANTO-NETO, H. & CAMILLI, J. A. 2011. Mechanical, biochemical and morphometric alterations in the femur of mdx mice. *Bone,* 48**,** 372-9.

NOVOTNY, S. A., WARREN, G. L., LIN, A. S., GULDBERG, R. E., BALTGALVIS, K. A. & LOWE, D. A. 2011. Bone is functionally impaired in dystrophic mice but less so than skeletal muscle. *Neuromuscul Disord,* 21**,** 183-93.

PASCA, L., GARDANI, A., PAOLETTI, M., VELARDO, D. & BERARDINELLI, A. 2022. Good response to the late treatment with ataluren in a boy with Duchenne muscular dystrophy: could the previous mild course of the disease have affected the outcome? *Acta Myol,* 41**,** 121-125.

PICKAR-OLIVER, A., GOUGH, V., BOHNING, J. D., LIU, S., ROBINSON-HAMM, J. N., DANIELS, H., MAJOROS, W. H., DEVLIN, G., ASOKAN, A. & GERSBACH, C. A. 2021. Full-length dystrophin restoration via targeted exon integration by AAV-CRISPR in a humanized mouse model of Duchenne muscular dystrophy. *Mol Ther,* 29**,** 3243-3257.

PONZETTI, M., UCCI, A., MAURIZI, A., GIACCHI, L., TETI, A. & RUCCI, N. 2022. Lipocalin 2 Influences Bone and Muscle Phenotype in the MDX Mouse Model of Duchenne Muscular Dystrophy. *Int J Mol Sci,* 23.

RAFAEL, J. A., TINSLEY, J. M., POTTER, A. C., DECONINCK, A. E. & DAVIES, K. E. 1998. Skeletal muscle-specific expression of a utrophin transgene rescues utrophin-dystrophin deficient mice. *Nat Genet,* 19**,** 79-82.

RAPAPORT, D., LEDERFEIN, D., DEN DUNNEN, J. T., GROOTSCHOLTEN, P. M., VAN OMMEN, G. J., FUCHS, O., NUDEL, U. & YAFFE, D. 1992. Characterization and cell type distribution of a novel, major transcript of the Duchenne muscular dystrophy gene. *Differentiation,* 49**,** 187-93.

ROK, M., WONG, T. W. Y., MAINO, E., AHMED, A., YANG, G., HYATT, E., LINDSAY, K., FATEHI, S., MARKS, R., DELGADO-OLGUIN, P., IVAKINE, E. A. & COHN, R. D. 2023. Prevention of early-onset cardiomyopathy in Dmd exon 52-54 deletion mice by CRISPR-Cas9-mediated exon skipping. *Mol Ther Methods Clin Dev,* 30**,** 246-258.

RUFO, A., DEL FATTORE, A., CAPULLI, M., CARVELLO, F., DE PASQUALE, L., FERRARI, S., PIERROZ, D., MORANDI, L., DE SIMONE, M., RUCCI, N., BERTINI, E., BIANCHI, M. L., DE BENEDETTI, F. & TETI, A. 2011. Mechanisms inducing low bone density in Duchenne muscular dystrophy in mice and humans. *J Bone Miner Res,* 26**,** 1891-903.

RUGGIERO, L., IODICE, R., ESPOSITO, M., DUBBIOSO, R., TOZZA, S., VITALE, F., SANTORO, L. & MANGANELLI, F. 2018. One-year follow up of three Italian patients with Duchenne muscular dystrophy treated with ataluren: is earlier better? *Ther Adv Neurol Disord,* 11**,** 1756286418809588.

RYU, S. M., KOO, T., KIM, K., LIM, K., BAEK, G., KIM, S. T., KIM, H. S., KIM, D. E., LEE, H., CHUNG, E. & KIM, J. S. 2018. Adenine base editing in mouse embryos and an adult mouse model of Duchenne muscular dystrophy. *Nat Biotechnol,* 36**,** 536-539.

SACCO, P., JONES, D. A., DICK, J. R. & VRBOVA, G. 1992. Contractile properties and susceptibility to exercise-induced damage of normal and mdx mouse tibialis anterior muscle. *Clin Sci (Lond),* 82**,** 227-36.

SAOUDI, A., ZARROUKI, F., SEBRIE, C., IZABELLE, C., GOYENVALLE, A. & VAILLEND, C. 2021. Emotional behavior and brain anatomy of the mdx52 mouse model of Duchenne muscular dystrophy. *Dis Model Mech,* 14.

SWIDERSKI, K., BROCK, C. J., TRIEU, J., CHEE, A., THAKUR, S. S., BAUM, D. M., GREGOREVIC, P., MURPHY, K. T. & LYNCH, G. S. 2021. Phosphorylation of ERK and dystrophin S3059 protects against inflammation-associated C2C12 myotube atrophy. *Am J Physiol Cell Physiol,* 320**,** C956-C965.

SWIDERSKI, K. & LYNCH, G. S. 2021. Murine models of Duchenne muscular dystrophy: is there a best model? *Am J Physiol Cell Physiol,* 321**,** C409-C412.

SWIDERSKI, K., MARTINS, K. J., CHEE, A., TRIEU, J., NAIM, T., GEHRIG, S. M., BAUM, D. M., BRENMOEHL, J., CHAU, L., KOOPMAN, R., GREGOREVIC, P., METZGER, F., HOEFLICH, A. & LYNCH, G. S. 2016. Skeletal muscle-specific overexpression of IGFBP-2 promotes a slower muscle phenotype in healthy but not dystrophic mdx mice and does not affect the dystrophic pathology. *Growth Horm IGF Res,* 30-31**,** 1-10.

SWIDERSKI, K., SHAFFER, S. A., GALLIS, B., ODOM, G. L., ARNETT, A. L., SCOTT EDGAR, J., BAUM, D. M., CHEE, A., NAIM, T., GREGOREVIC, P., MURPHY, K. T., MOODY, J., GOODLETT, D. R., LYNCH, G. S. & CHAMBERLAIN, J. S. 2014. Phosphorylation within the cysteine-rich region of dystrophin enhances its association with beta-dystroglycan and identifies a potential novel therapeutic target for skeletal muscle wasting. *Hum Mol Genet,* 23**,** 6697-711.

TINSLEY, J., DECONINCK, N., FISHER, R., KAHN, D., PHELPS, S., GILLIS, J. M. & DAVIES, K. 1998. Expression of full-length utrophin prevents muscular dystrophy in mdx mice. *Nat Med,* 4**,** 1441-4.

TU, H., QIAN, J., ZHANG, D., BARKSDALE, A. N., WADMAN, M. C., PIPINOS, II & LI, Y. L. 2022. Different responses of skeletal muscles to femoral artery ligation-induced ischemia identified in BABL/c and C57BL/6 mice. *Front Physiol,* 13**,** 1014744.

TUNG, J. Y., LAM, T. P. & CHAN, S. H. 2021. Bone microarchitectural alterations in boys with Duchenne muscular dystrophy on long-term glucocorticoid treatment. *J Bone Miner Metab,* 39**,** 606-611.

VAI, S., BIANCHI, M. L., MORONI, I., MASTELLA, C., BROGGI, F., MORANDI, L., ARNOLDI, M. T., BUSSOLINO, C. & BARANELLO, G. 2015. Bone and Spinal Muscular Atrophy. *Bone,* 79**,** 116-20.

VAN PUTTEN, M., PUTKER, K., OVERZIER, M., ADAMZEK, W. A., PASTEUNING-VUHMAN, S., PLOMP, J. J. & AARTSMA-RUS, A. 2019. Natural disease history of the D2-mdx mouse model for Duchenne muscular dystrophy. *FASEB J,* 33**,** 8110-8124.

VEILLEUX, L. N. & RAUCH, F. 2017. Muscle-Bone Interactions in Pediatric Bone Diseases. *Curr Osteoporos Rep,* 15**,** 425-432.

VOIT, A., PATEL, V., PACHON, R., SHAH, V., BAKHUTMA, M., KOHLBRENNER, E., MCARDLE, J. J., DELL'ITALIA, L. J., MENDELL, J. R., XIE, L. H., HAJJAR, R. J., DUAN, D., FRAIDENRAICH, D. & BABU, G. J. 2017. Reducing sarcolipin expression mitigates Duchenne muscular dystrophy and associated cardiomyopathy in mice. *Nat Commun,* 8**,** 1068.

WADA, E., HAMANO, T., MATSUI, I., YOSHIDA, M., HAYASHI, Y. K. & MATSUDA, R. 2019. Renal involvement in the pathogenesis of mineral and bone disorder in dystrophin-deficient mdx mouse. *J Physiol Sci,* 69**,** 661-671.

WANG, Z., KUHR, C. S., ALLEN, J. M., BLANKINSHIP, M., GREGOREVIC, P., CHAMBERLAIN, J. S., TAPSCOTT, S. J. & STORB, R. 2007. Sustained AAV-mediated dystrophin expression in a canine model of Duchenne muscular dystrophy with a brief course of immunosuppression. *Mol Ther*, 15**,** 1160-6.

WARD, L. M., HADJIYANNAKIS, S., MCMILLAN, H. J., NORITZ, G. & WEBER, D. R. 2018. Bone Health and Osteoporosis Management of the Patient With Duchenne Muscular Dystrophy. *Pediatrics*, 142**,** S34-S42.

WATANABE, H., NUMATA, K., ITO, T., TAKAGI, K. & MATSUKAWA, A. 2004. Innate immune response in Th1- and Th2-dominant mouse strains. *Shock*, 22**,** 460-6.

WONG, T. W. Y., AHMED, A., YANG, G., MAINO, E., STEIMAN, S., HYATT, E., CHAN, P., LINDSAY, K., WONG, N., GOLEBIOWSKI, D., SCHNEIDER, J., DELGADO-OLGUIN, P., IVAKINE, E. A. & COHN, R. D. 2020. A novel mouse model of Duchenne muscular dystrophy carrying a multi-exonic Dmd deletion exhibits progressive muscular dystrophy and early-onset cardiomyopathy. *Dis Model Mech*, 13.

WOOD, C. L., SUCHACKI, K. J., VAN 'T HOF, R., CAWTHORN, W. P., DILLON, S., STRAUB, V., WONG, S. C., AHMED, S. F. & FARQUHARSON, C. 2020. A comparison of the bone and growth phenotype of mdx, mdx:Cmah(-/-) and mdx:Utrn(+/-) murine models with the C57BL/10 wild-type mouse. *Dis Model Mech*, 13.

XIONG, Y., ZHOU, Y. & JARRETT, H. W. 2009. Dystrophin glycoprotein complex-associated Gbetagamma subunits activate phosphatidylinositol-3-kinase/Akt signaling in skeletal muscle in a laminin-dependent manner. *J Cell Physiol*, 219**,** 402-14.

YOUNG, C. N. J., GOSSELIN, M. R. F., RUMNEY, R., OKSIEJUK, A., CHIRA, N., BOZYCKI, L., MATRYBA, P., LUKASIEWICZ, K., KAO, A. P., DUNLOP, J., ROBSON, S. C., ZABLOCKI, K. & GORECKI, D. C. 2020. Total Absence of Dystrophin Expression Exacerbates Ectopic Myofiber Calcification and Fibrosis and Alters Macrophage Infiltration Patterns. *Am J Pathol*, 190**,** 190-205.

YOUNG, C. S., MOKHONOVA, E., QUINONEZ, M., PYLE, A. D. & SPENCER, M. J. 2017. Creation of a Novel Humanized Dystrophic Mouse Model of Duchenne Muscular Dystrophy and Application of a CRISPR/Cas9 Gene Editing Therapy. *J Neuromuscul Dis*, 4**,** 139-145.

ZHANG, Y., LI, H., MIN, Y. L., SANCHEZ-ORTIZ, E., HUANG, J., MIREAULT, A. A., SHELTON, J. M., KIM, J., MAMMEN, P. P. A., BASSEL-DUBY, R. & OLSON, E. N. 2020. Enhanced CRISPR-Cas9 correction of Duchenne muscular dystrophy in mice by a self-complementary AAV delivery system. *Sci Adv,* 6**,** eaay6812.

Figures

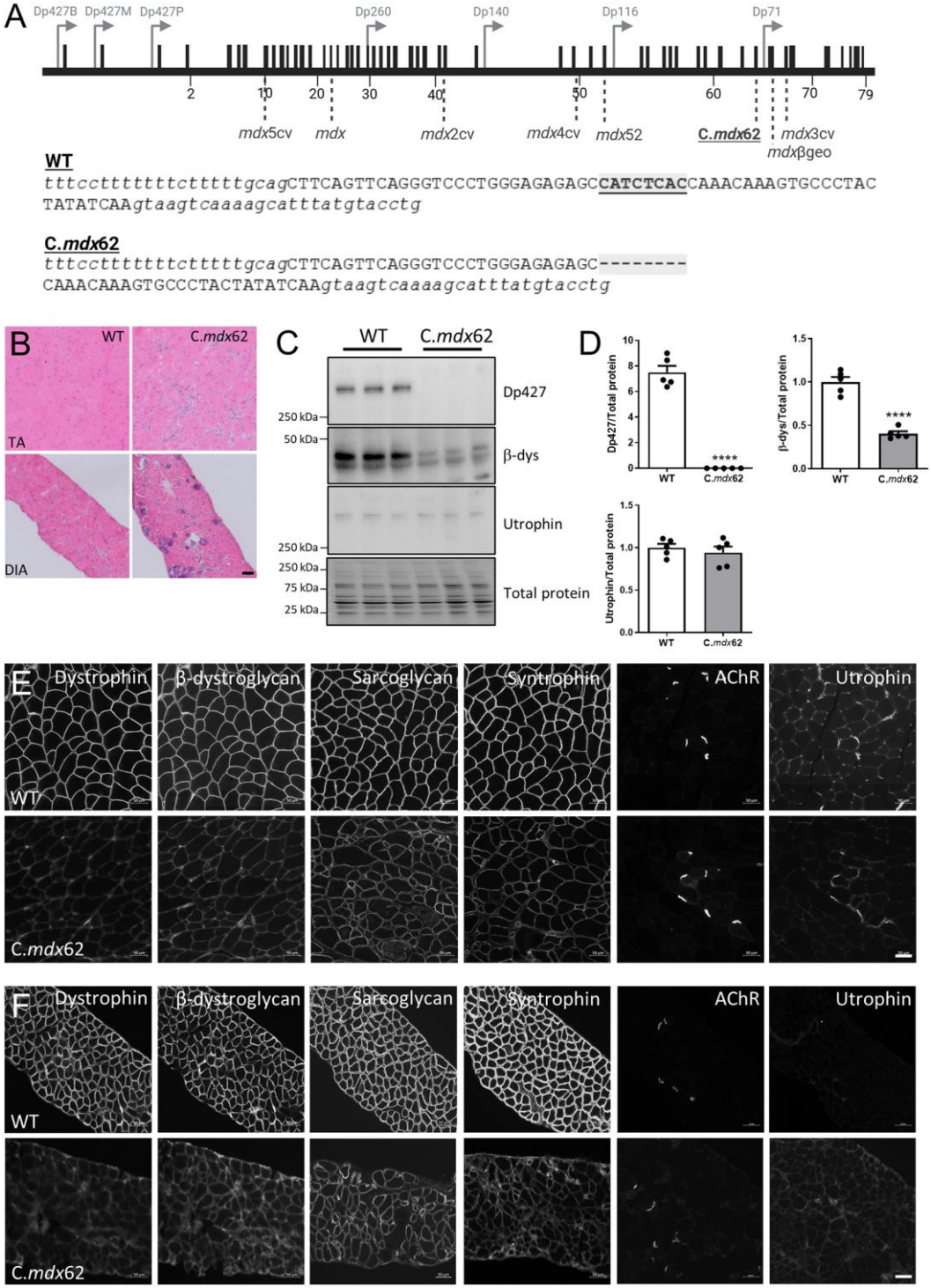

Fig. 1. C.*mdx*62 mice lack dystrophin and have reduced DGC protein expression at the sarcolemma of skeletal muscle fibers. (**A**) Top, Schematic of dystrophin gene sequence. Black boxes represent exons, grey arrows show promoter locations for different dystrophin

isoforms. Light grey dotted lines indicate locations of reported mutations in DMD mouse models including the C.*mdx*62. Bottom, Schematic of exon 62 (capital letters) flanked by intron 61 and intron 62 (lower case) showing the 8 bp deletion within exon 62 in the C.*mdx*62 mice (highlighted and underlined) relative to the WT sequence. Created with BioRender.com. (**B**) Representative hematoxylin and eosin-stained sections of TA muscle and diaphragm from a 3-month-old WT and C.*mdx*62 mouse. Scale bar = 50 µm. (**C**) Representative western immunoblots from lysates prepared from gastrocnemius muscles from 3-month-old WT and C.*mdx*62 mice (n = 5 mice/genotype) were analyzed for dystrophin (Dp427), β-dystroglycan, and utrophin protein expression shown with total protein stain imaged on stain-free gels. (**D**) Levels of dystrophin (Dp427), β-dystroglycan, and utrophin protein were quantified relative to total protein. Data are presented as mean ± SEM. Statistical analysis using a two tailed Student's t-test. ****$P < 0.0001$. Representative sections of TA muscle (**E**) and diaphragm (**F**) from a 3-month-old WT and C.*mdx*62 mouse immunostained for dystrophin, β-dystroglycan, sarcoglycan, syntrophin, acetylcholine receptor (AChR), and utrophin. Scale bar = 50 µm.

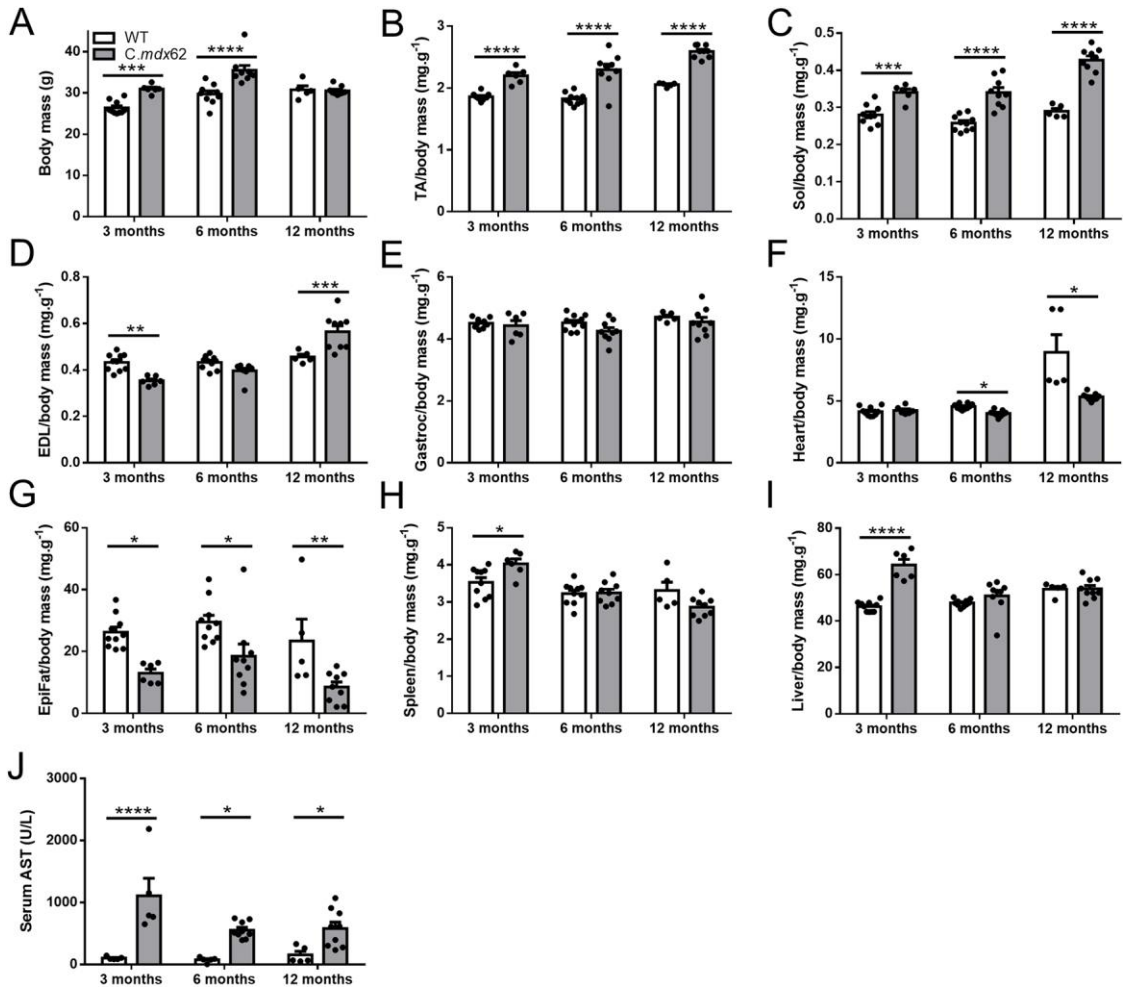

Fig. 2. C.*mdx*62 mice exhibit skeletal muscle hypertrophy, reduced epididymal fat mass, and increased serum markers of muscle damage. Male WT and C.*mdx*62 mutant mice were killed at 3 months (n = 10 and n = 6 mice/genotype respectively), 6 months (n = 10 and n = 9 mice/genotype respectively), and 12 months of age (n = 5 and n = 9 mice/genotype respectively) and assessed for body mass (**A**) as well as mass of the TA (**B**), soleus (**C**), EDL (**D**), and gastrocnemius (**E**) muscles, the heart (**F**), epididymal fat pad (**G**), spleen (**H**), and liver (**I**) mass relative to body mass. (**J**) Serum was assessed for AST levels. Data are presented as mean ± SEM. Statistical analysis using a two-way ANOVA with a post-hoc Bonferroni's test, with the exception of the heart data which were analyzed using a Mann-Whitney U test due to a non-normal distribution. **P* < 0.05, ***P* < 0.01, ****P* < 0.001, *****P* < 0.0001 relative to age-matched WT mice.

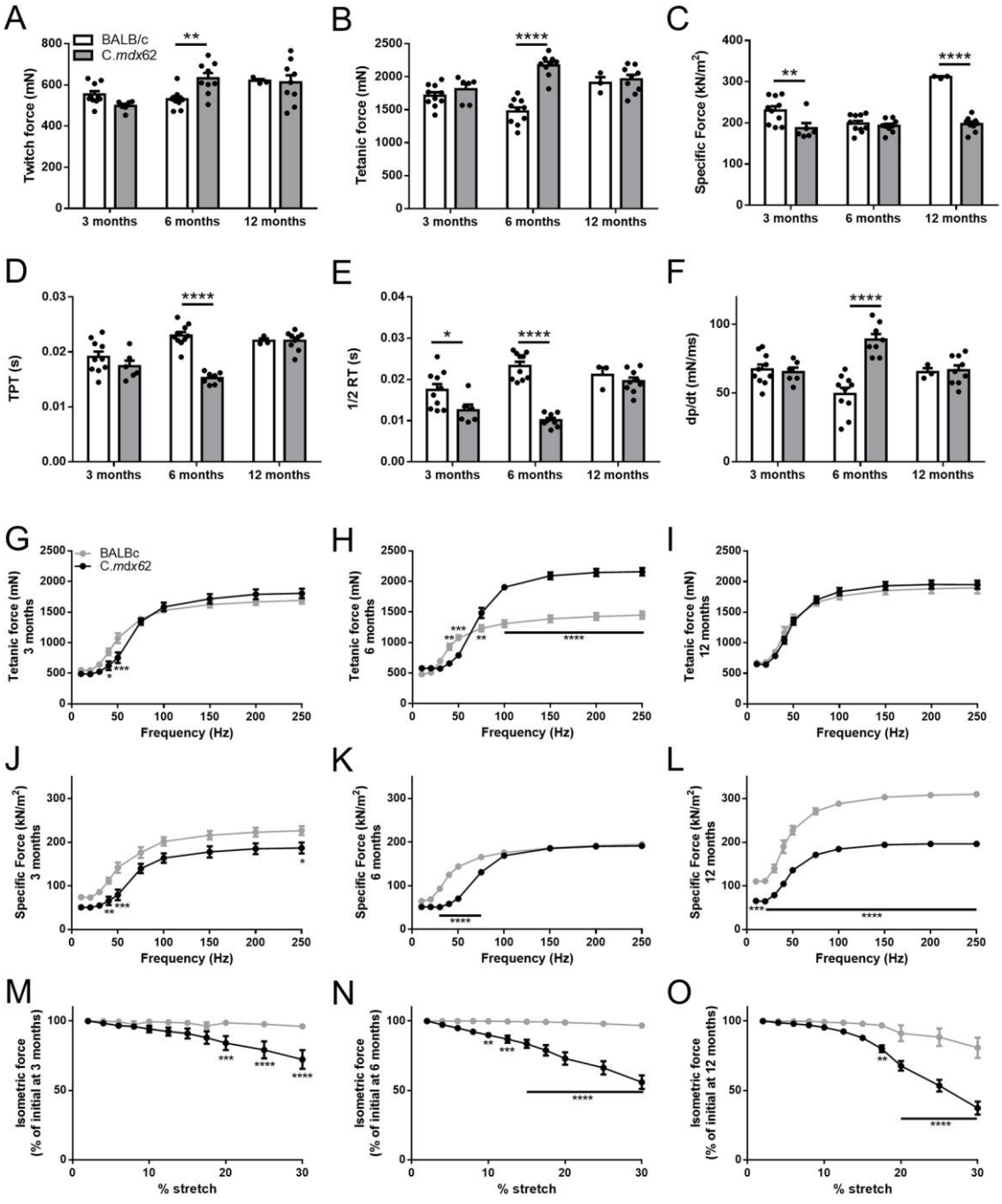

Fig. 3. Contractile properties of TA muscles from 3, 6, and 12 month old WT and C.*mdx*62 mice. Functional parameters of the TA muscle from male 3-, 6-, and 12-month-old WT (n = 10, n = 10, n = 3 mice/age group respectively) and C.*mdx*62 mutant (n = 5, n = 9, n = 9 mice/age group respectively) mice were assessed *in situ* for maximum twitch force (**A**), maximum tetanic force (**B**), specific force (**C**), time-to-peak twitch (**D**), one-half relaxation time (**E**), and maximum rate of twitch contraction (**F**). Statistical analysis using a two-way ANOVA with a post-hoc Bonferroni's test. The frequency-force relationship to determine maximal force (**G-I**) and specific (normalized) force (**J-L**) were determined over

a range of stimulation frequencies (10-250 Hz) at the various ages. The cumulative force deficit associated with repeated lengthening contractions was used to assess the muscle susceptibility to contraction-mediated injury in 3-month-old (**M**), 6-month-old (**N**), and 12-month-old (**O**) mice. Data are presented as mean ± SEM. Statistical analysis using a repeated measures two-way ANOVA with a post-hoc Bonferroni's test. **P* < 0.05, ***P* < 0.01, ****P* < 0.001, *****P* < 0.0001 relative to age-matched WT.

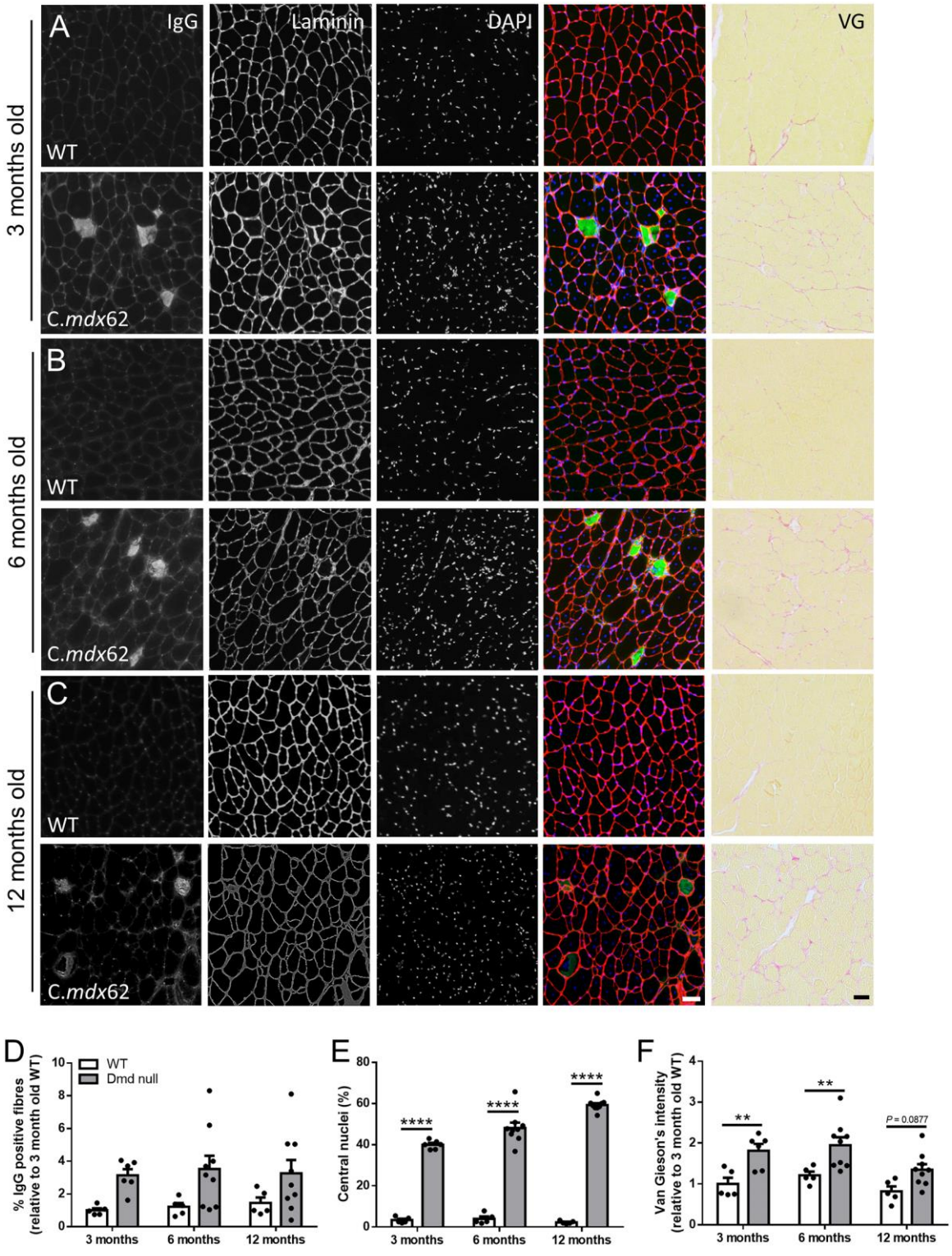

Fig. 4. IgG infiltration, central nuclei, and fibrosis are increased in TA muscles of C.*mdx*62 mice. Male WT and C.*mdx*62 mutant mice were killed at 3 months (n = 5 and n = 6 mice/genotype respectively) (**A**), 6 months (n = 5 and n = 9 mice/genotype respectively) (**B**), and 12 months of age (n = 5 and n = 9 mice/genotype respectively) (**C**). TA muscles were excised, sectioned, and immunostained for IgG (green), laminin (red), and DAPI

(blue), or stained with Van Gieson's. Scale bar = 50 µm. Sections were quantified to determine the percentage of IgG infiltrated muscle fibers (**D**), the number of muscle fibers containing central nuclei (**E**), or the area of Van Gieson's staining (**F**). Data are presented as mean ± SEM. Statistical analysis using a two-way ANOVA with a post-hoc Bonferroni's test. $^{**}P < 0.01$, $^{****}P < 0.0001$ relative to age-matched WT mice.

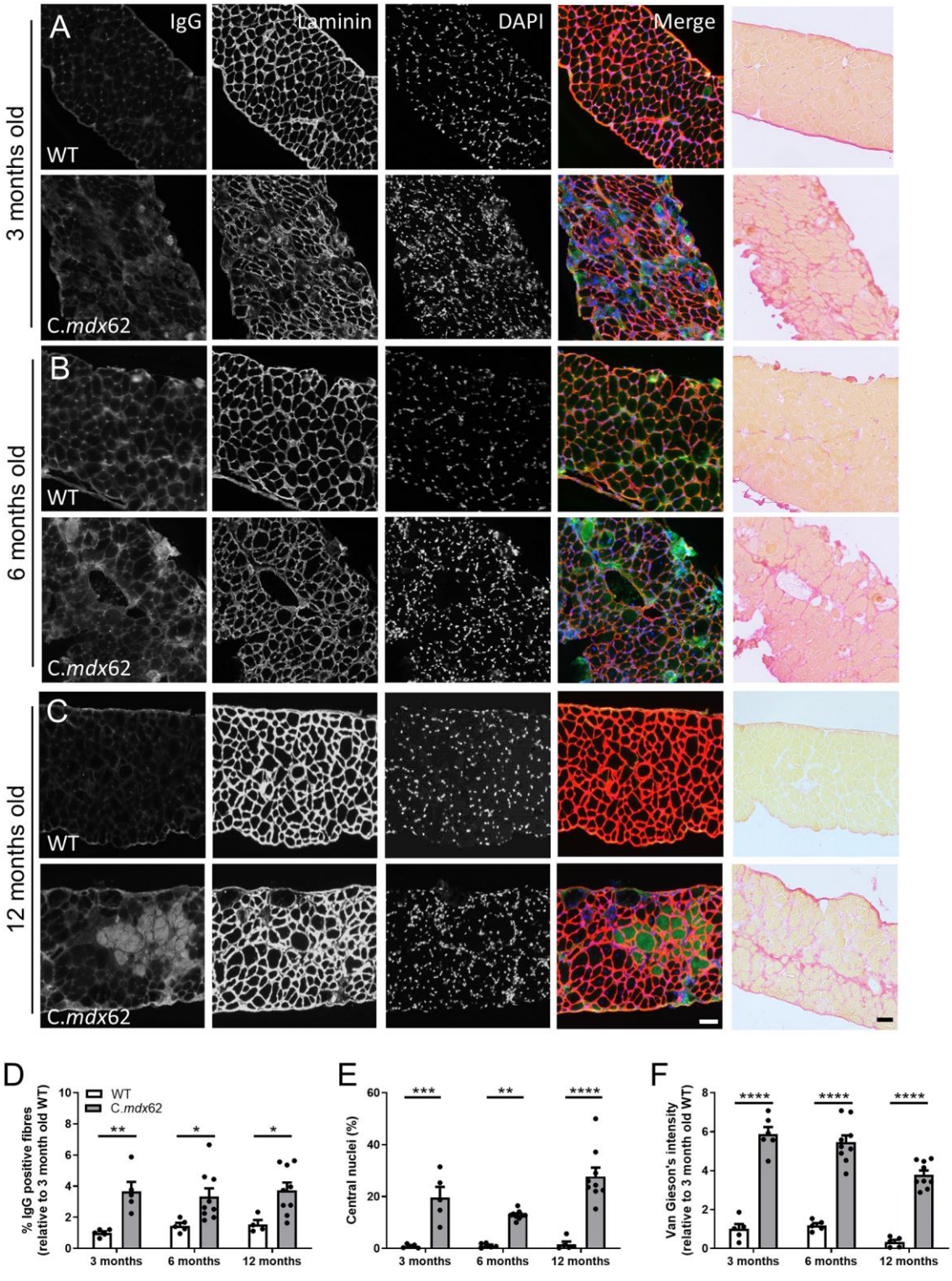

Fig. 5. IgG infiltration, central nuclei, and fibrosis are increased in the diaphragm of C.*mdx*62 mice. Male WT and C.*mdx*62 mutant mice were killed at 3 months (n = 5 and n = 6 mice/genotype respectively) (**A**), 6 months (n = 5 and n = 9 mice/genotype respectively) (**B**), and 12 months (n = 5 and n = 9 mice/genotype respectively) of age (**C**). Diaphragm muscles were excised, sectioned, and immunostained for IgG (green), laminin (red), and DAPI (blue),

or stained with Van Gieson's. Scale bar = 50 µm. Sections were quantified to determine the percentage of IgG infiltrated muscle fibers (**D**), the number of muscle fibers containing central nuclei (**E**), or the area of Van Gieson's staining (**F**). Data are presented as mean ± SEM. Statistical analysis using a two-way ANOVA with a post-hoc Bonferroni's test. **P* < 0.05, ***P* < 0.01, ****P* < 0.001, *****P* < 0.0001 relative to age-matched WT mice.

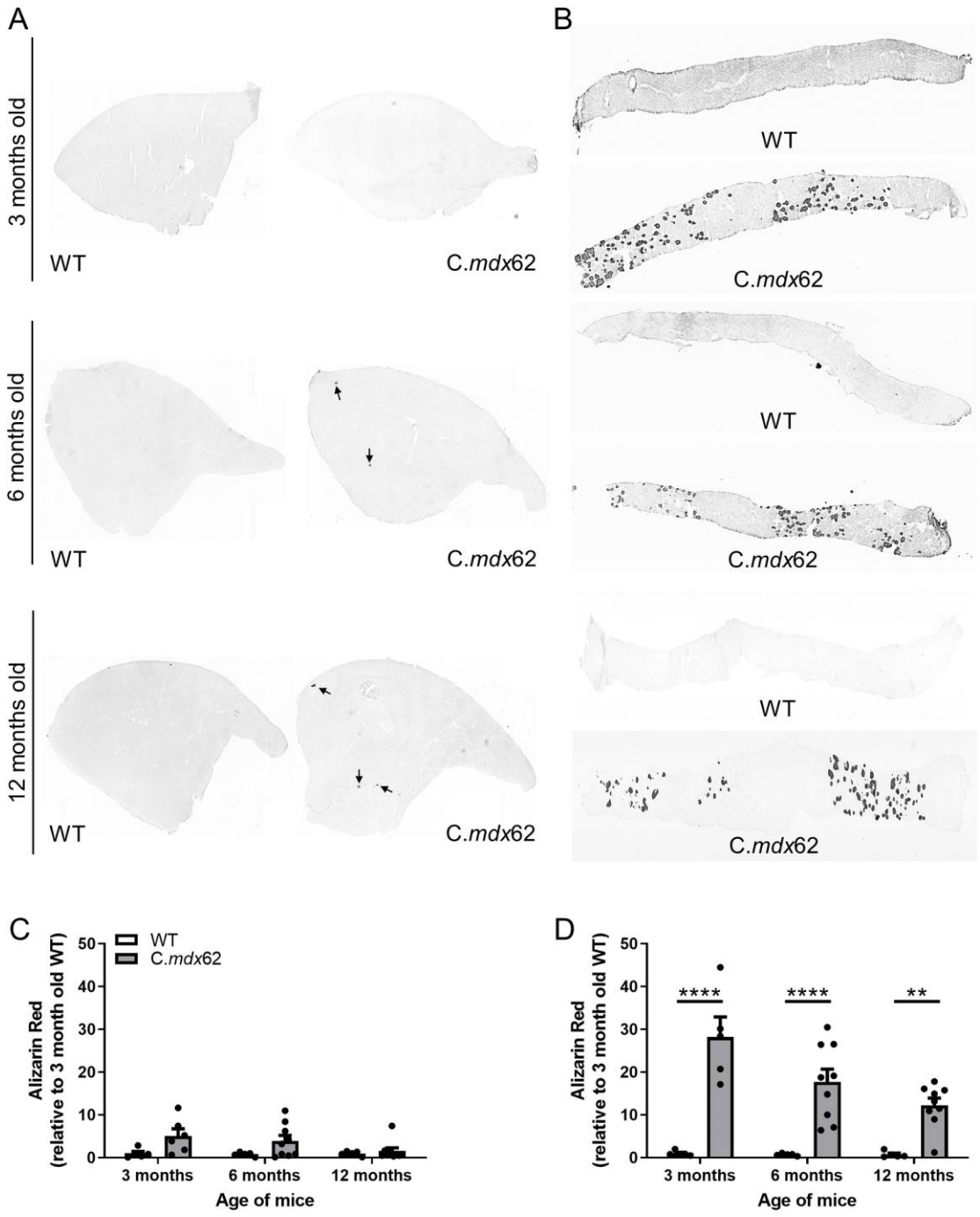

Fig. 6. Alizarin red staining shows heterotopic ossification in the TA and diaphragm muscles of C.*mdx*62 mice. Male WT and C.*mdx*62 mutant mice were killed at 3 months (n = 5 and n = 6 mice/genotype respectively), 6 months (n = 5 and n = 9 mice/genotype respectively), and 12 months of age (n = 5 and n = 9 mice/genotype respectively). TA (**A**) and diaphragm (**B**) muscles were excised, sectioned, and stained with Alizarin red for the presence of calcification. Sections were quantified to determine the intensity of Alizarin red staining in TA (C) and diaphragm (D) sections. Data are presented as mean ± SEM. Statistical analysis using a two-way ANOVA with a post-hoc Bonferroni's test. $^{**}P < 0.01$, $^{****}P < 0.0001$ relative to age-matched WT mice.

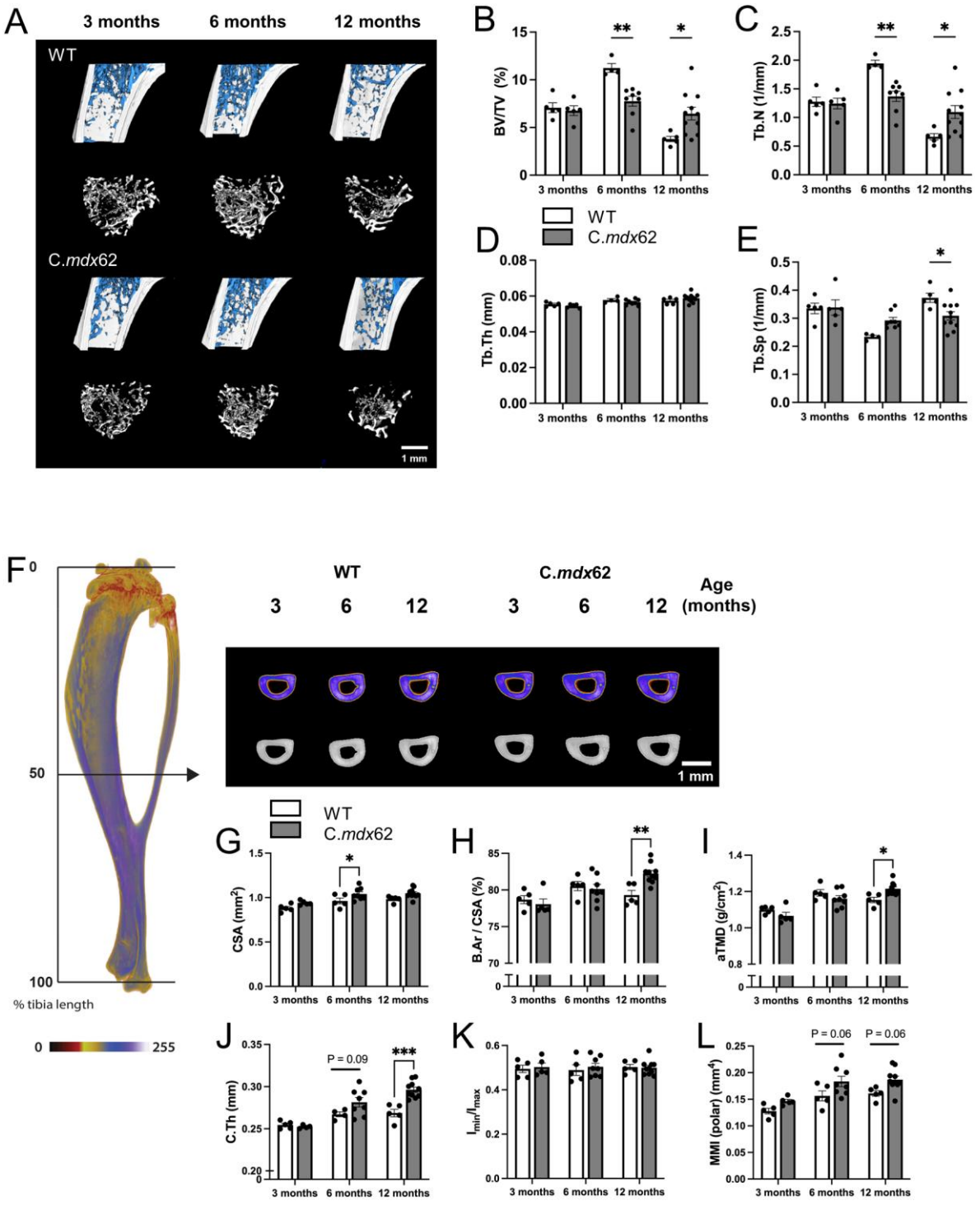

Fig. 7. Dystrophin deficiency delays trabecular bone mass accrual and alters cortical bone structure in C.*mdx*62 mice. Tibial bones were taken from male WT and C.*mdx*62 mutant mice were killed at 3 (n = 5 and n = 5 mice/group respectively), 6 (n = 5 and n = 8 mice/group respectively), and 12 (n = 5 and n = 10 mice/group respectively) months of age. Representative images for WT and C.*mdx*62 mice across 3, 6 and 12 months of age, with trabecular bone shown in blue (top row) or white (bottom row) for each genotype (**A**). Scale

bar represents 1 mm. Trabecular bone volume ratio (BV/TV, %) (**B**), trabecular number (Tb.N, 1/mm; **C**), trabecular thickness (Tb.Th, mm; **D**) and trabecular separation (Tb.Sp, 1/mm; **E**). Data are represented as mean ± SEM. Representative reconstructions are shown for WT and C.*mdx*62 mice at the tibial mid-diaphysis (50% of bone length), with a pseudodensity filter applied (top row) (**F**). Scale bar represents 1 mm. Cross-sectional area (CSA, mm^2, **G**), normalised bone area (%, **H**), areal tissue mineral density (aTMD, g/cm^2, **I**), cortical thickness (C.Th, mm, **J**), bone shape ratio (ratio between minimum and maximum principal moments of inertia, I_{min}/I_{max}; **I**) and polar moment of inertia (MMI, mm^4, **L**). Data are represented as mean ± SEM. Statistical significance using two-way ANOVA followed by Bonferroni multiple comparisons test, with $*P < 0.05$, $**P < 0.01$, $***P < 0.005$ relative to age-matched WT mice.

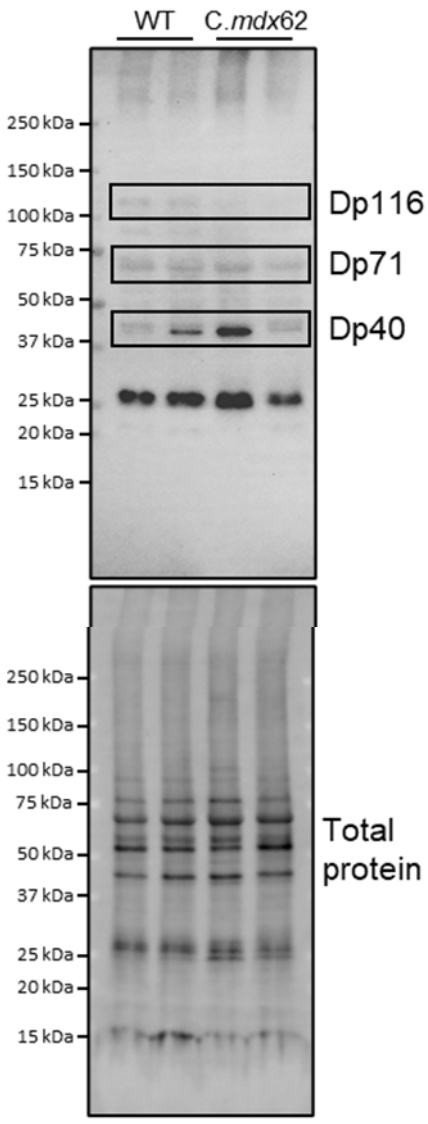

Supp. Fig. S1.

Fig. S1. C.*mdx*62 mice lack Dp116 but express Dp71 and Dp40. Sciatic nerve was dissected from 12-month-old BALB/c WT and C.*mdx*62 mice, protein extracted, and western immunoblotting undertaken to assess levels of Dp116, Dp71, and Dp40 dystrophin protein isoforms. Total protein was detected using the BioRad stain-free blot chemistry to confirm equal protein loading across samples.

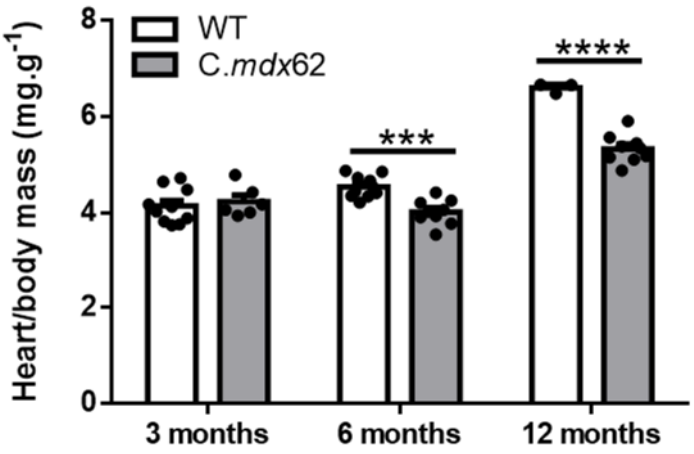

Supp. Fig. S2.

Fig. S2. C.*mdx*62 heart mass is reduced at 6 and 12 months of age. Data from Figure 2F with the two abnormally large hearts removed from the 12 month old WT group confirming reduced normalize heart mass in the C.*mdx*62 mouse at 6 and 12 months of age. Data are presented as mean ± SEM. Statistical analysis using a two-way ANOVA with a post-hoc Bonferroni's test (with n = 3-10 mice/age/genotype). ***$P < 0.001$, ****$P < 0.0001$ relative to age-matched WT mice.

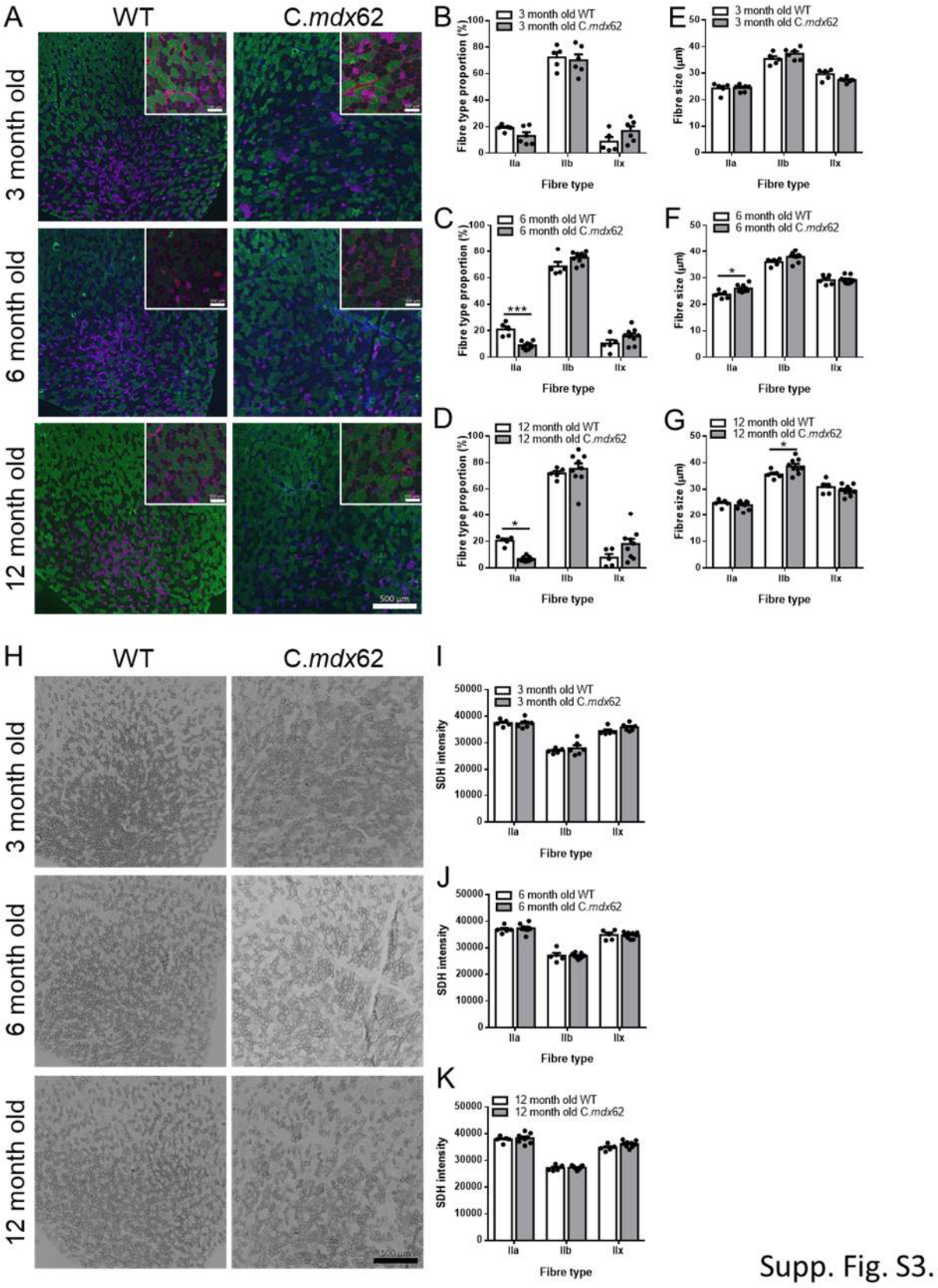

Supp. Fig. S3.

Fig. S3. Muscle fiber type analysis in 3, 6, and 12 month old WT and C.*mdx*62 mice.

WT and C.*mdx*62 mutant mice were killed at 3, 6, and 12 months of age. TA muscles were excised, sectioned, and immunostained for type IIa (purple), type IIb (green), type IIx (black) muscle fibers, laminin (red), DAPI (nuclei, blue) (**A**). Stained sections were analyzed to determine the fiber type proportions (**B-D**) and fiber size (**E-G**). Sections were also immunoreacted for and for SDH (bright field) to assess oxidative capacity (**H**) and quantified for SDH intensity (**I-K**) of the different fiber types. Scale bar = 500 µm (100 µm for insets). Data are presented as mean ± SEM. Statistical analysis using a two-way ANOVA with a post-hoc Bonferroni's test (with n = 5-9 mice/age/genotype). $*P < 0.05$, $***P < 0.001$ relative to age-matched WT mice.

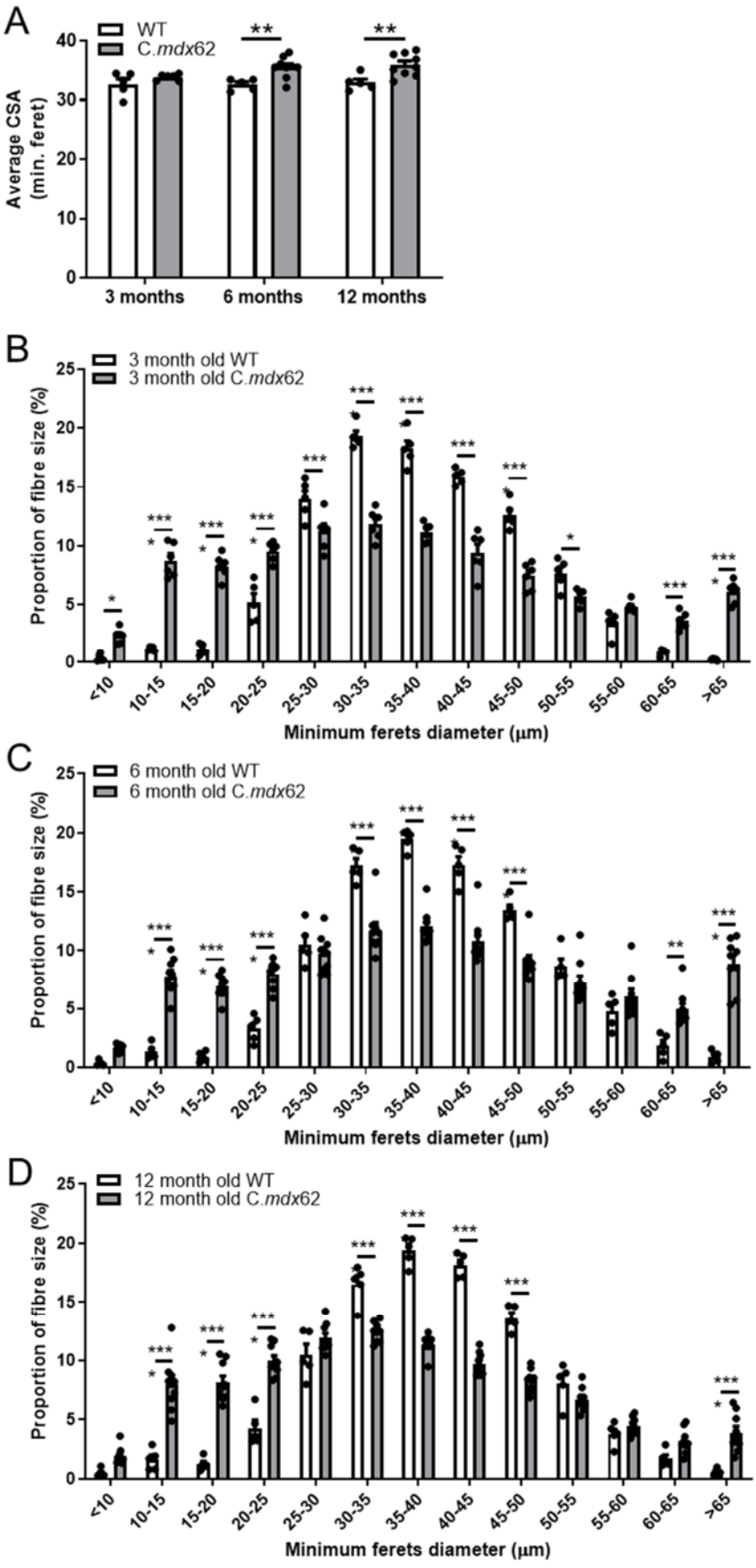

Supp. Fig. S4.

Fig. S4. C.*mdx*62 mice exhibit variable (and increased) muscle fiber size at 3, 6, and 12 months of age. WT and C.*mdx*62 mutant mice were killed at 3, 6, and 12 months of age. TA muscles were excised, sectioned, and immunostained for laminin. Stained sections were analyzed to determine average fiber size (CSA; **A**), as well as the size distribution of muscle fibers from 3 (**B**), 6 (**C**), and 12 (**D**) month old mice. Data are presented as mean ± SEM. Statistical analysis using a two-way ANOVA with a post-hoc Bonferroni's test (with n = 5-9 mice/age/genotype). *$P < 0.05$, **$P < 0.01$, ***$P < 0.001$, ****$P < 0.0001$ relative to age-matched WT mice.

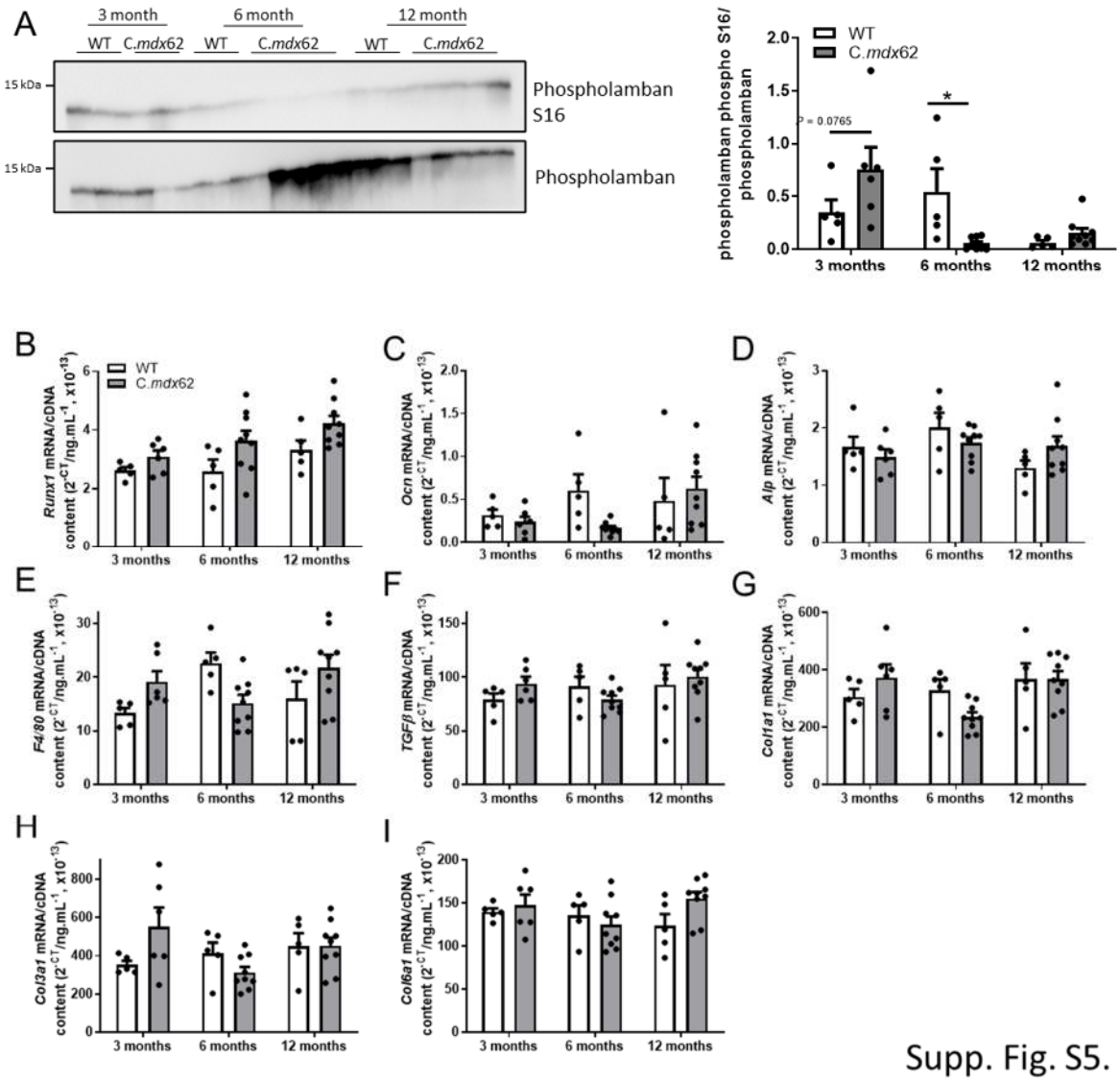

Fig. S5. C.*mdx*62 mice exhibit SERCA dysfunction in the heart. WT and C.*mdx*62 mutant mice were killed at 3, 6, and 12 months of age. Hearts were excised and protein and RNA extracted for analysis. (**A**) Protein was assessed for levels of phosphorylated and total phospholamban. cDNA was analyzed by qRT-PCR for mRNA expression of (**B**) *Runx1*, (**C**) *Ocn*, (**D**) *Alp*, (**E**) *F4/80*, (**F**) *Tgfβ*, (**G**) *Col1a1*, (**H**) *Col3a1*, and (**I**) *Col6a1*. Data are presented as mean ± SEM. Statistical analysis using a two-way ANOVA with a post-hoc Bonferroni's test (with n = 5-9 mice/age/genotype). *$P < 0.05$ relative to age-matched WT mice.

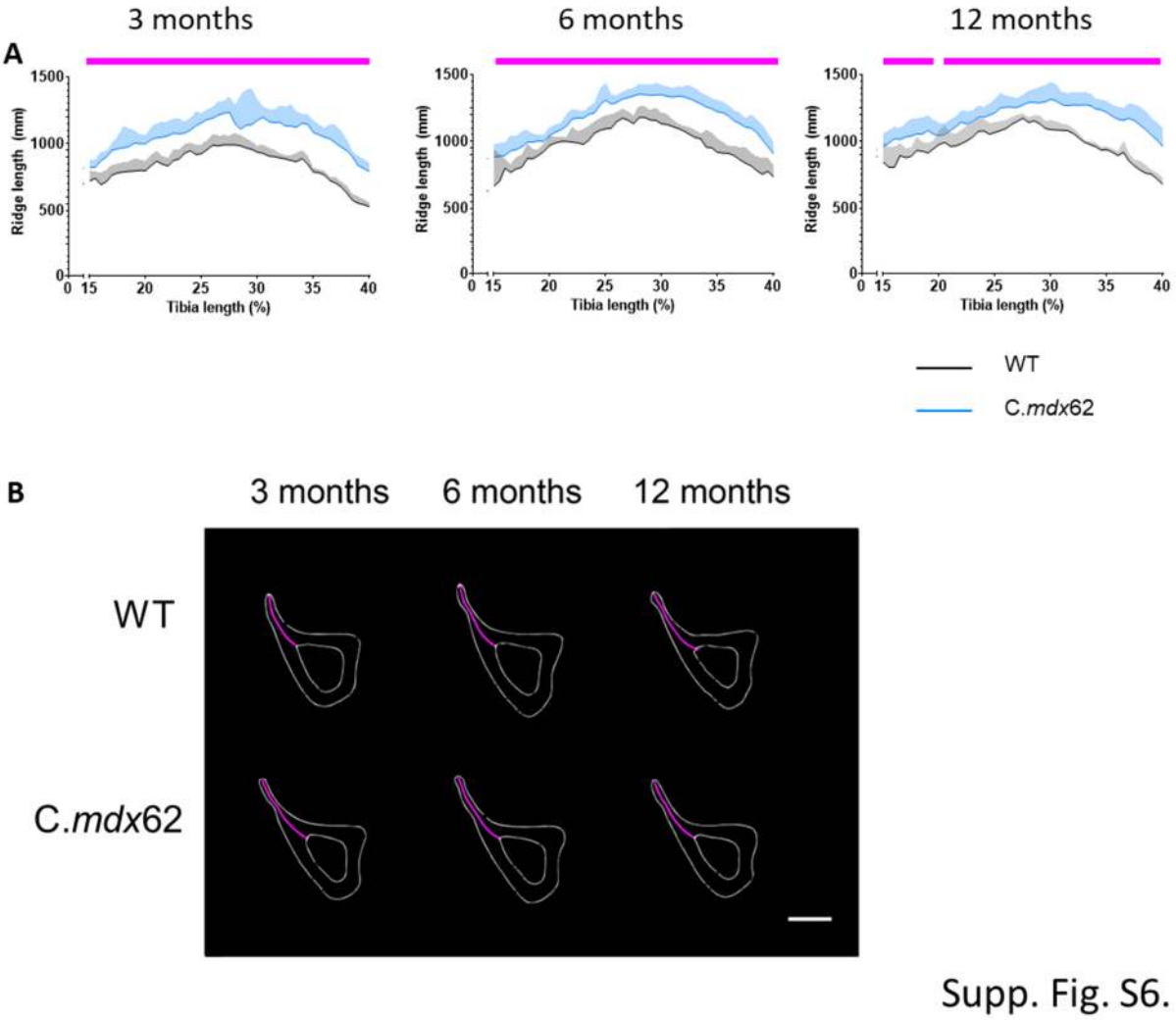

Fig. S6. Augmentation of the tibial crest during skeletal development in C.*mdx*62 mice. (**A**) Tibial crest length was measured using a customized macro plugin in ImageJ. Data + STD for BALB/c wildtype (WT) and C.*mdx*62 mice are represented in black and blue, respectively. Significant effects ($p<0.05$) are indicated by the solid pink bar above each graph, as determined by repeated measures two-way ANOVA with correction for multiple comparisons by the two-stage step-up method of Benjamini, Krieger, and Yekutieli (36). (**B**) Representative binary cross-sectional images are shown at 30% tibial length in WT and C.*mdx*62 mice at 3, 6 and 12 months of age. Periosteal (outer) and endocortical (inner) surfaces are outlined in white, and the tibial crest length is outlined in pink. Scale bar represents 1 mm.